Universität Zürich[UZH]

Search for a heavy resonance decaying into a Z boson and a Higgs boson

Master Thesis

Mathematisch-naturwissenschaftliche Fakultät

der

Universität Zürich

Pascal Bärtschi

Adviser

Prof. Dr. Benjamin Kilminster,

Dr. Alberto Zucchetta

Zürich

June 2020

Abstract

The observation of the Higgs boson with a mass of 125 GeV by the CMS and ATLAS experiments leads to a conundrum called the hierarchy problem, which cannot be explained by the standard model. Many models including Supersymmetry, composite and little Higgs try to explain the hierarchy problem. The composite and little Higgs models can be tested by looking for charged and neutral heavy resonances, as predicted by the heavy-vector-triplet models. This thesis describes the search for a neutral heavy resonance produced through $q\bar{q}$ annihilation or vector boson fusion and decaying to a Z boson and a standard model Higgs boson. The Z boson is identified through its leptonic decay channels (electrons, muons or neutrinos) and the Higgs boson through its mass and the presence of b quarks. The search is performed in the boosted regime for heavy resonances with masses between 800 GeV and 5 TeV. The data from proton-proton collisions was collected in 2016, 2017 and 2018 by the CMS Collaboration at a center-of-mass energy of 13 TeV, corresponding to an combined integrated luminosity of 137.37 fb^{-1}. No significant excesses are found. The mass range below 3.4 and 3.7 TeV can be excluded at a 95% confidence level if the heavy resonance couples predominantly to fermions and bosons, respectively. If the heavy resonances couple exclusively to the standard model bosons, a Z' cross section smaller than 0.4-24 fb is excluded, depending on the Z' mass.

Contents

1 Introduction

The standard model cannot explain why the weak force is 10^{24} times stronger than gravity or why the observed Higgs boson mass is so small. Supersymmetry, composite and little-Higgs models give different answers to explain these conundrums. This thesis describes the search for a neutral heavy resonance as predicted by heavy-vector-triplet (HVT) models, in order to test composite and little-Higgs theories. The search is performed by looking for the signal of neutral heavy resonances produced through $q\bar{q}$ annihilation or vector boson fusion and decaying to a Z boson and a Higgs boson. The Z boson is identified by its leptonic decays into pairs of electrons, muons or neutrinos. The neutrinos cannot be measured in the detector, therefore this decay channel is identified through their large missing transverse energy in the detector. The Higgs boson is identified by its mass and the decay to b quarks.
An earlier search for a heavy resonance with the same decay signatures conducted by the CMS collaboration with 2016 data did not find any significant excess and excluded a mass range below 2.1 or 2.3 TeV at a 95% confidence level, depending on whether the neutral heavy resonance couples predominately to fermions and bosons, respectively [1]. The ATLAS collaboration conducted a similar search, not finding any significant excess and excluding the neutral heavy resonance mass range below 1.5 TeV for both models at a 95% confidence level [2]. The search is performed with data measured in the CMS detector in 2016, 2017 and 2018 at a center-of-mass energy of 13 TeV, corresponding to an integrated luminosity of 35.9 fb^{-1}, 41.5 fb^{-1} and 59.97 fb^{-1}, respectively. This amounts to four times more statistics than used in the earlier search conducted by the CMS collaboration. Additionally the inclusive decay channel of the Higgs boson and the vector boson fusion production of the heavy resonance are taken into account to increase the sensitivity.
The thesis is structured as follows. The theoretical motivation for the search is explained in chapter 2. Chapter 3 describes the CMS detector and the collection of data. In chapter 4 the used datasets and simulated signal and background models are described. The reconstruction of the physics objects and bosons from the data measured in the detector is explained in chapter 5 and 6, respectively. Chapter 7 focuses on the selection of event candidates for this analysis. The top-quark background contribution has to be normalized with data, which is described in chapter 8. Chapter 9 describes the background estimation and chapter 10 the modelling of the signal. Chapter 11 discusses the systematic uncertainties. The results are shown in chapter 12. A summary is given in the final chapter 13.

2 Theoretical motivation

The standard model of particle physics (SM), shown in Fig. 1, describes all known elementary particles. The particles are classified either as half-integer-spin fermions or integer-spin bosons with spin referring to the intrinsic angular momentum of the particles. The quarks carry color charge and interact via the strong interaction by exchanging gluons. Because of color confinement, such that only colorless particles can exist, quarks form composite particles called hadrons. A meson is formed by a quark pair and three quarks form a baryon. The quarks as well as the charged leptons carry electromagnetic charge and weak isospin, and can interact via the electromagnetic interaction by exchanging photons, and via the weak interaction by exchanging W and Z bosons. The neutrinos only interact via the weak interaction, which makes it extremely difficult to detect them. The fermions can be classified into three groups, each with successively higher masses. The bosons are divided into spin-1 gauge bosons and a spin-0 scalar boson. The gauge bosons are the mediators of the electromagnetic, strong and weak interactions. The gravitational interaction is not described in the standard model. The Higgs boson is the manifestation of a scalar field, which causes particles to acquire mass. The Higgs boson was predicted by Higgs [3], Englert and Brout [4], and Guralnik, Hagen and Kibble [5] in order to explain the electroweak symmetry breaking. The Higgs boson was discovered in 2012 by the ATLAS and CMS experiments [6][7].

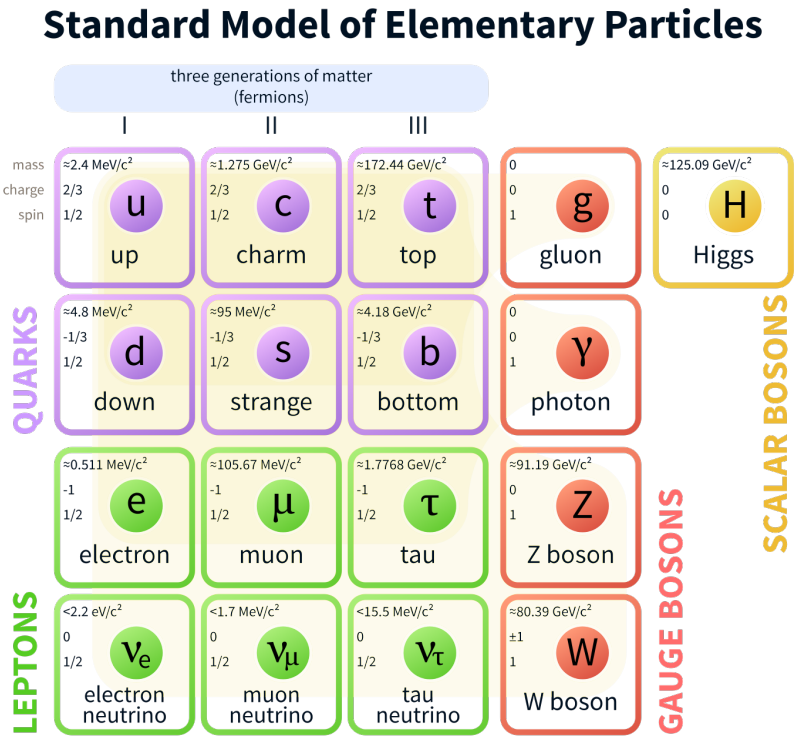

Figure 1: Standard Model of particle physics. Taken from [8].

The Higgs boson can be produced through gluon fusion, vector boson fusion, in

association with Z or W bosons, or in association with top quarks as shown in Figure 2.

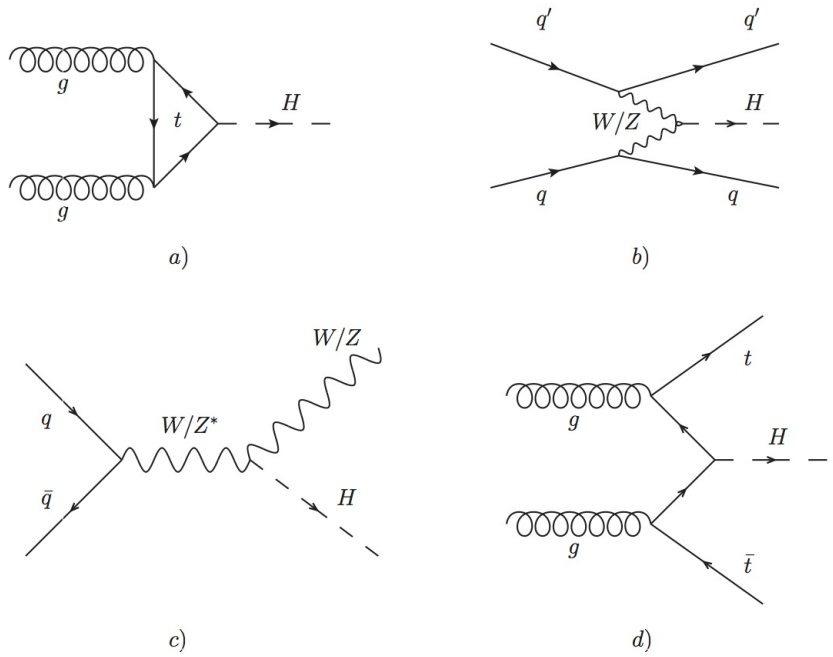

Figure 2: Higgs boson production channels: a) gluon fusion, b) vector boson fusion, c) in association with Z or W bosons, d) in association with top quarks.

The Higgs boson has the following decay modes, ordered in decreasing branching ratio at 125 GeV: $b\bar{b}$, W^+W^-, gg, $\tau^+\tau^-$, $c\bar{c}$, ZZ, $\gamma\gamma$, $Z\gamma$ and $\mu\mu$. The branching ratios are shown in Figure 3.

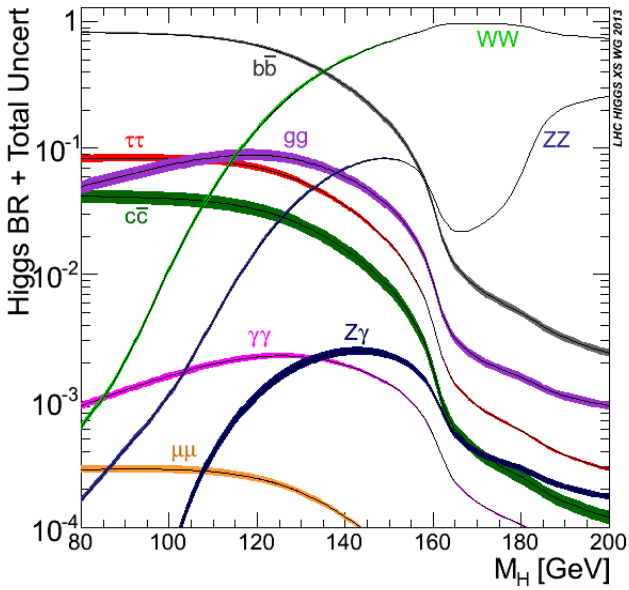

Figure 3: Branching ratio of Higgs boson decay modes. Retrieved from [9].

The Higgs boson has been observed in five decay modes: $\gamma\gamma$, ZZ, W^+W^-, $\tau^+\tau^-$ and $b\bar{b}$. The excess is most significant in the Higgs boson decay to $\gamma\gamma$ and ZZ, because of the good mass resolution in these decay channels. The Higgs boson to $b\bar{b}$ decay has the largest branching fraction at 125 GeV, but the signal gets overwhelmed by b quarks from QCD background. The QCD background is suppressed if the Higgs boson is required to be in the boosted regime, such that it has high p_T. For the Higgs boson to $b\bar{b}$ search the production associated with a Z or W boson has the highest sensitivity. Combining the results from all production channels [10][11][12] the ATLAS and CMS Collaborations discovered the Higgs boson decaying to $b\bar{b}$ in 2018 [13][14].

The standard model describes the current knowledge about the elementary particles, but it cannot explain the hierarchy problem, made apparent by the weak force being 10^{24} times stronger than gravity. This violates naturalness, which assumes that all forces should be of the same order of magnitude. The discovery of the Higgs boson with a mass of 125 GeV creates another unsolved complication. The masses of particles with interactions like the Higgs boson get corrections from quantum loops:

$$(m_H{}^{obs})^2 = m_H{}^2 + \Delta m_H{}^2. \tag{1}$$

The main contribution to the Higgs boson mass correction comes from the top quark, which is the heaviest fermion.

$$\Delta m_H{}^2 = -\frac{|\lambda_t|^2}{8\pi} \cdot \Lambda^2 + ..., \tag{2}$$

where λ_t is the Yukawa coupling between the top quark and the Higgs boson and Λ is the cut-off scale up to which the standard model is valid. If Λ is large, say at the order of the Planck scale where the coupling strength of gravity becomes of comparable strength to the other interactions, the correction grows drastically. In order to get the measured Higgs boson mass, a fine-tuning cancellation is needed to balance out the large correction. The hierarchy problem can be fixed by assuming yet-undiscovered particles, which would remove the necessity of fine-tuning. A theory called supersymmetry predicts a superpartner for each SM particle. The spin of these superpartners differ by half of a unit, so SM fermions and bosons would be accompanied by supersymmetric bosons and fermions, respectively. Important for the hierarchy problem is the superpartner of the top quark, called the stop quark. The top-quark loop would be cancelled out with the stop-quark loop, prevent the correction to the Higgs boson mass from increasing drastically. Other theories, called composite Higgs [15, 16, 17] and little-Higgs [18, 19, 20] consider the Higgs boson as a low-energy bound state of an unknown strongly interacting sector. The bound state is expected to form at the TeV scale, therefore the Higgs boson has to be interpreted as a pseudo-Goldstone boson to allow a mass below the TeV scale. Every time a continuous symmetry is spontaneously broken a massless Goldstone boson appears [21][22][23]. If the symmetry is not exact, a pseudo-Goldstone boson appears, which has a small mass instead of being massless. An example of pseudo-Goldstone bosons are pions [24]. They appear because of the spontaneous breaking of the chiral-flavor

symmetry of QCD, which is not an exact symmetry due to the mass of the quarks. The Composite-Higgs theories can be tested by looking for other bound states at the TeV scale. Heavy Vector Triplet (HVT) models predict narrow resonances of spin-1 at the TeV scale: charged W' and neutral Z' [25]. The models feature two different scenarios: Model A and B assume the new physics to couple preferably to light fermions and standard model bosons, respectively. In Fig. 4 the branching fractions as a function of the resonance mass are shown for model A and B. The benchmark model B is of particular interest for this analysis, as it features a branching fraction of 50% for the decay to a Z boson and a Higgs boson. Additionally we have the heavy resonance produced through Vector Boson Fusion, which we label as model C.

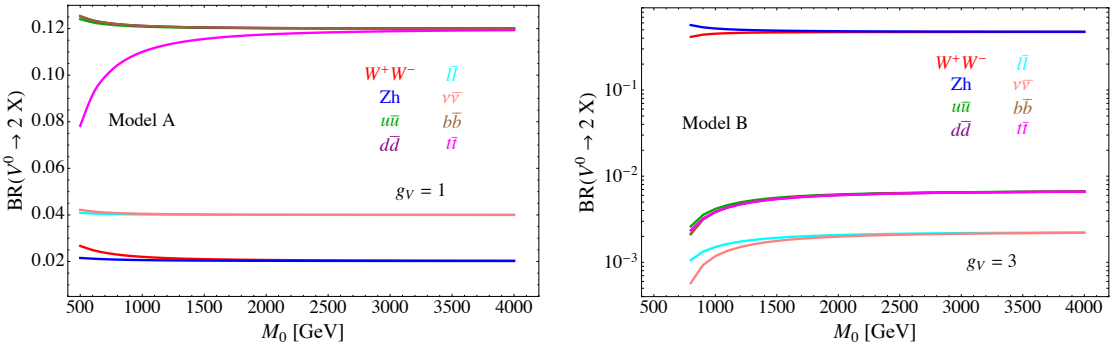

Figure 4: Branching ratios as a function of the resonance mass for the HVT benchmark model A (Left) and model B (Right) [25].

3 The CMS experiment

CERN is the European Organization for Nuclear Research near Geneva at the French-Swiss border. The Large Hadron Collider (LHC) at CERN is a powerful particle accelerator in which two particle beams (protons or heavy ions) travel in opposite directions through a 27 km long circular tunnel at close to the speed of light. The beams are brought into collision along the circular path at 4 detectors: CMS, ATLAS, LHCb, and ALICE. CMS and ATLAS are general-purpose detectors with research topics ranging from studying the standard model to searching for extra dimensions and dark matter [26][27]. LHCb is constructed to detect particles in one direction and its main research topics are measurements of CP violation and rare decays of B hadrons [28]. ALICE is dedicated to the research of quark-gluon plasma [29]. Figure 5 shows an illustration of the LHC with the four main experiments.

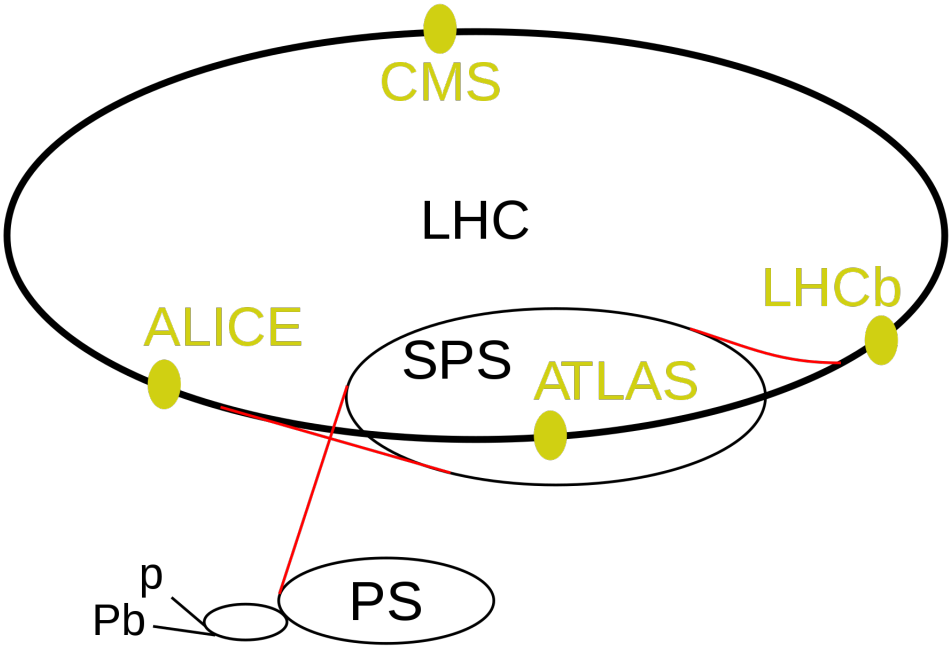

Figure 5: Illustration of the LHC with the four interaction points. Taken from [30].

3.1 CMS Detector

The CMS detector is placed 100 m underground near the french village of Cessy. It weighs about 14'000 tons, is 21 metres long, 15 metres wide and 15 metres high. The detector is composed of different subdetectors and has two different sections: the barrel and the end caps. The barrel section is built in order radially outward from the beam axis and is used to measure particles transverse to the beam axis. The end caps are placed on either end of the detector in order to extend the solid angle coverage and capture very forward particles. The detector subsystems radially outward from the beam axis are a tracker to measure the tracks of charged particles, an electromagnetic

calorimeter (ECAL) for measuring the energy of electrons and photons, a hadronic calorimeter (HCAL) to measure the energy of hadrons, a superconducting solenoid inducing a magnetic field of 3.8 Tesla and the muon chambers for measuring the muons [26]. An illustration of the detector with its subsystems is shown in Figure 6.

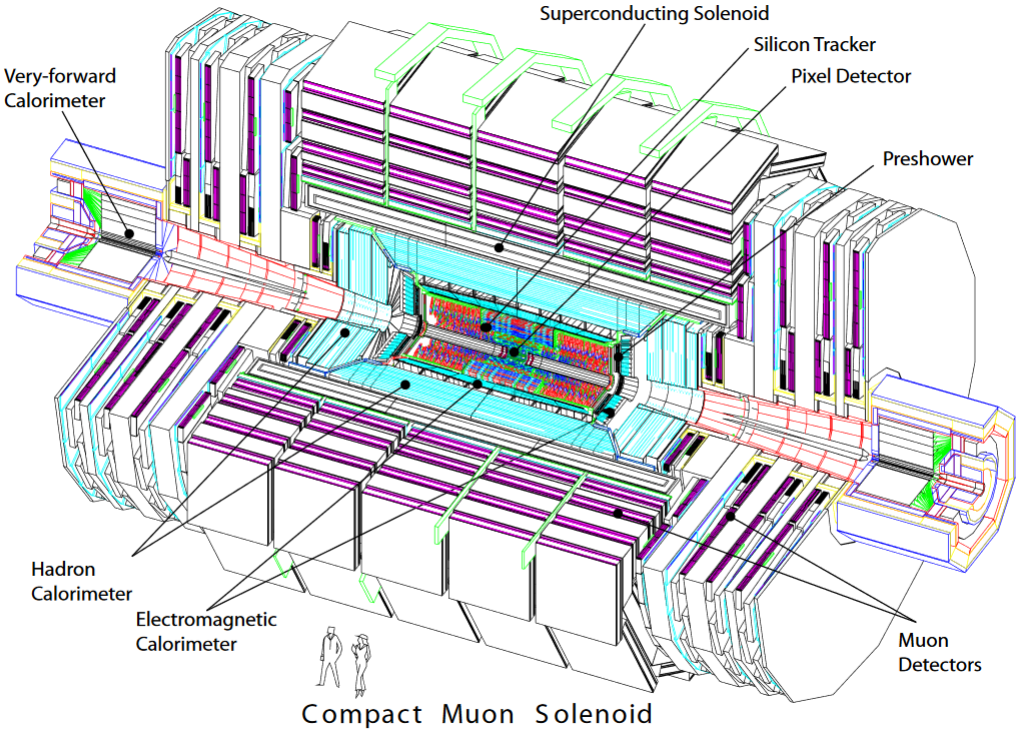

Figure 6: Illustration of the CMS detector. Taken from [26].

3.1.1 Coordinate system

Figure 7 shows the coordinate system used to describe particles in the detector [26]. The protons move in the positive and negative z-directions and collide in the center of the detector. x and y define a plane, which is perpendicular to the beam axis and is called the transverse plane. The angle in the transverse plane is denoted by ϕ, and θ is the angle with respect to the plane formed by the x and z direction. The component of the momentum in the transverse plane is called transverse momentum p_T and is used because the momentum of the partons in the proton that produce the collision is not known in the z direction.

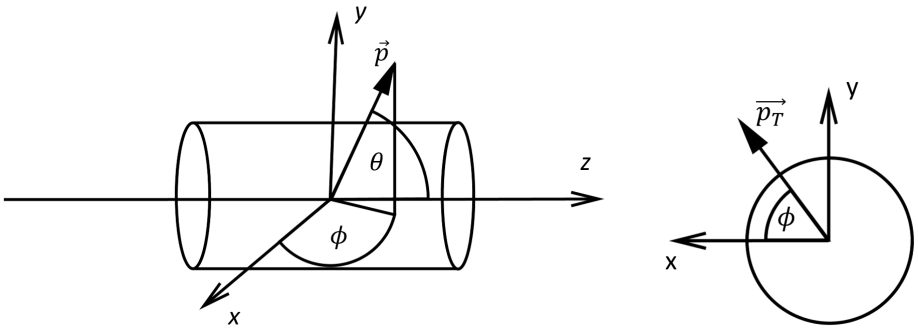

Figure 7: Cylindrical coordinate system of a collider detector.

Instead of the angle θ, the pseudorapidity η is used, which is defined as a function of θ by

$$\eta = -ln\left[\tan\left(\frac{\theta}{2}\right)\right] . \tag{3}$$

Figure 8 shows the relation between θ and η.

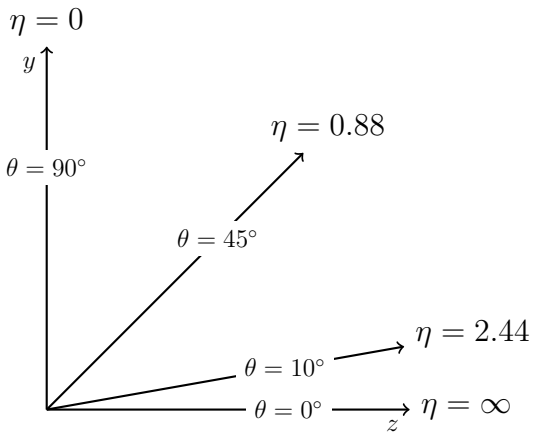

Figure 8: Pseudorapidity.

3.1.2 Tracker system

The tracker system consists of a silicon pixel and a silicon strip detector as shown in Fig. 9 and has a coverage for charged particles of $|\eta| < 2.5$. The pixel detector is closest to the interaction point and important for the vertex reconstruction due to its good spatial resolution. The pixel detector was upgraded in the shutdown of LHC at the end of 2016 due to radiation damage and to increase the readout bandwidth, which is needed for good tracking efficieny with the increased luminosity of LHC. The pixel detector is built from 124 million silicon pixels distributed over 4 barrel layers and 3 endcap disks at each end. Before the upgrade, the pixel detector consisted of 66 million pixels distributed on 3 layers and 2 disks. The barrel layers

are 53 cm long and the innermost layer has a radial distance of 29 mm and the outer layer 16 cm to the beam axis [31]. The spatial resolution of 10 μm transversally and 30 μm longitudinally result in a position resolution of 10-12 μm in each spatial dimension for vertex reconstruction [32]. This resolution makes it possible to find a secondary vertex as in the decay of b quarks, described in 5.8.

The silicon strip detector has a larger spatial resolution than the pixel detector and is used to measure the momentum of charged particles from the curved track due to the magnetic field. The inner strip detector consists of silicon strips distributed on 4 barrel layers (TIB) and 3 disks at the endcaps (TID). The outer strip detector is built from 6 cylinders with silicon strips mounted on rods (TOB). There are 9 disks mounted with silicon strips placed at the endcaps (TEC). In total the strip detector consists of 9.3 million silicon strips with a hit resolution of 10-50 μm, increasing with the radius from the beam axis [32].

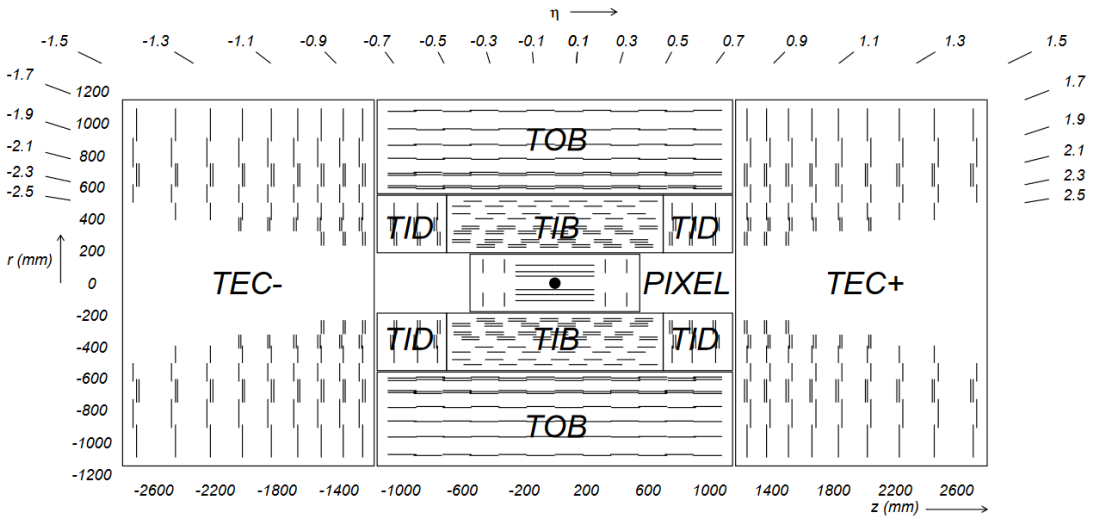

Figure 9: Schematic of the CMS tracker system with the pixel detector before the upgrade in 2017. Taken from [33].

3.1.3 Electromagnetic calorimeter

The electromagnetic calorimeter (ECAL) is used to measure the energy of electrons and photons. The electrons and photons induce electromagnetic showers, which is a cascade of electrons and photons, whose energy is absorbed in the calorimeter. The calorimeter is built from 61200 lead tungstate ($PbWO_4$) crystals projecting radially in the barrel region and 7324 crystals in the two endcaps. The ECAL has a coverage of $|\eta| < 3$. A preshower detector is placed in front of the endcaps, built from lead radiators with silicon strip sensors placed on top of each radiator to measure the deposited energy and transverse shower profile. The preshower detector is used to measure forward π^0 mesons, which predominantly decay to two photons. The lead tungstate crystals have a high density, allowing a compact calorimeter with fine granularity to be built. The crystals in the barrel and endcap region have a length of 230 mm and 220 mm, corresponding to 25.8 and 24.7 radiation lengths, respectively.

The calorimeter needs to be fast in order to avoid overlapping signals from different bunch crossings. Therefore the scintillation decay time of the crystals is of the same order of magnitude as the LHC bunch crossing time, which is 25 ns. The scintillation light is measured with photodetectors mounted on top of each crystal. In the barrel region avalanche photodiodes, and at the endcaps vacuum phototriodes are used. The energy resolution for a 20 GeV electron is around 0.9% and decreases to 0.35% for 300 GeV or higher [26].

3.1.4 Hadronic calorimeter

The hadronic calorimeter (HCAL) is used to measure the deposited energy of hadrons. The hadrons induce hadronic showers by inelastic hadronic interactions, which cause the production of mostly light mesons. The neutral pions decay to photon pairs and induce an electromagnetic shower. The HCAL is a sampling calorimeter, made out of alternating layers of steel or brass absorbers and plastic scintillators. The scintillation light is guided with wavelength shifting fibers and measured with hybrid photodiodes. The HCAL inside of the solenoid does not offer sufficient interaction lengths to capture all the energy of hadronic showers. Therefore an outer calorimeter is placed outside of the solenoid. The barrel and endcap section allow a coverage of $|\eta| < 3$. A forward calorimeter is placed 11.15 m from the interaction point to increase the coverage to $|\eta| < 5$. The particle flux is much higher for the forward calorimeter than for the rest of the detector. Therefore the forward calorimeter is built from steel plates and quartz fibres. The energy resolution for a jet with $p_T > 30$ GeV is around 15-20% and decreases to 10% for $p_T > 100$ GeV [34].

3.1.5 Muon chambers

The outer part of the detector and also its largest part are the muon chambers. They have a radial distance of 4 m to the beam line and extend to 7.3 m. The muon chambers consist of four barrel wheels and four endcaps disks, separated by iron flux-return yokes to contain the magnetic field inside the detector. The flux-return yokes also serve as hadron absorbers. The muon chambers consist of different types of gaseous detectors, depending on the magnetic field and the rate of particle flux. In the barrel region the magnetic field is uniform and small, and the rate of neutron-induced background and muons is low. In the endcap region on the other hand the magnetic field is non-uniform and large, as is the rate of background and muons. Therefore drift tube chambers distributed on 4 cylinders are used in the barrel region and cathode strip chambers in the endcap region. The spatial resolution of the drift tube chambers is 80-120 μm and 40-150 μm for the cathode strip chambers [35]. Resistive plate chambers are added both in the barrel and endcap regions to ensure a good trigger efficiency at higher collision rates. They have a coarse spatial resolution of 0.8-1.2 cm, but fast readout and a good time resolution. The muon chambers have a coverage of $|\eta| < 2.4$ and allow the identification of muons with an efficiency of 95% for energies larger than a few GeV. The muon momentum resolution is 1-6% for muons with $p_T < 100$ GeV and around 10% for $p_T < 1$ TeV [36].

3.2 Data collection

The protons in the LHC are divided in to 2556 bunches per beam, which collide at a rate of 40 MHz in the CMS detector. The beam intensity is quantified using the instantaneous luminosity $\mathcal{L}$, which takes the number of protons per bunch, the frequency of collisions and the cross-sectional area into account. The instantaneous luminosity reached in Run 2 is $\mathcal{L} = 2 \times 10^{34} \mathrm{cm}^{-2}\mathrm{s}^{-1}$, as shown in Fig. 10. Numerous proton-proton collisions take place per bunch crossing, most of them are soft collisions not interesting for physics analysis. The mean number of interactions per crossing is called pile-up and is shown for each year in Figure 12. The average pile-up increased from 23 in 2016 to 32 in 2018 because of the increased instantaneous luminosity. A trigger system is used to store only the most interesting events. The Level-1 trigger uses coarse measurements from the calorimeters and muon detectors and makes a fast decision to reduce the rate down to 100 kHz. Then the High Level Trigger (HLT) performs a more complex selection and stores the events on disk at a rate of a few hundered Hz [37]. The amount of recorded data is quantified by the integrated luminosity, which is shown in Fig. 11 for the years 2015 to 2018.

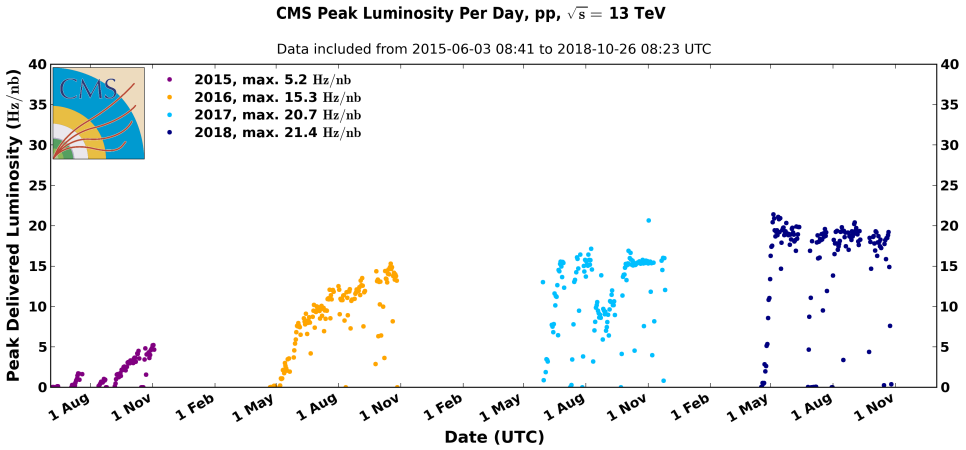

Figure 10: Peak instantaneous luminosity per day for 2015 to 2018. Taken from [38].

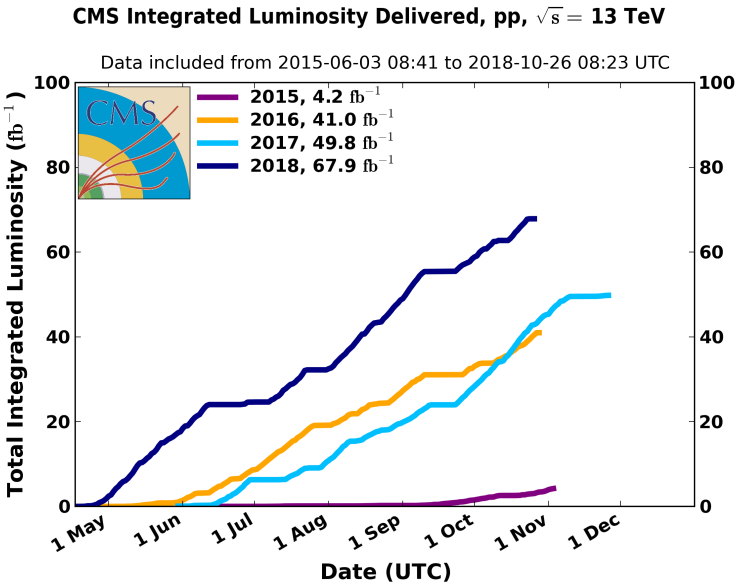

Figure 11: Integrated luminosity for 2015 to 2018. Taken from [38].

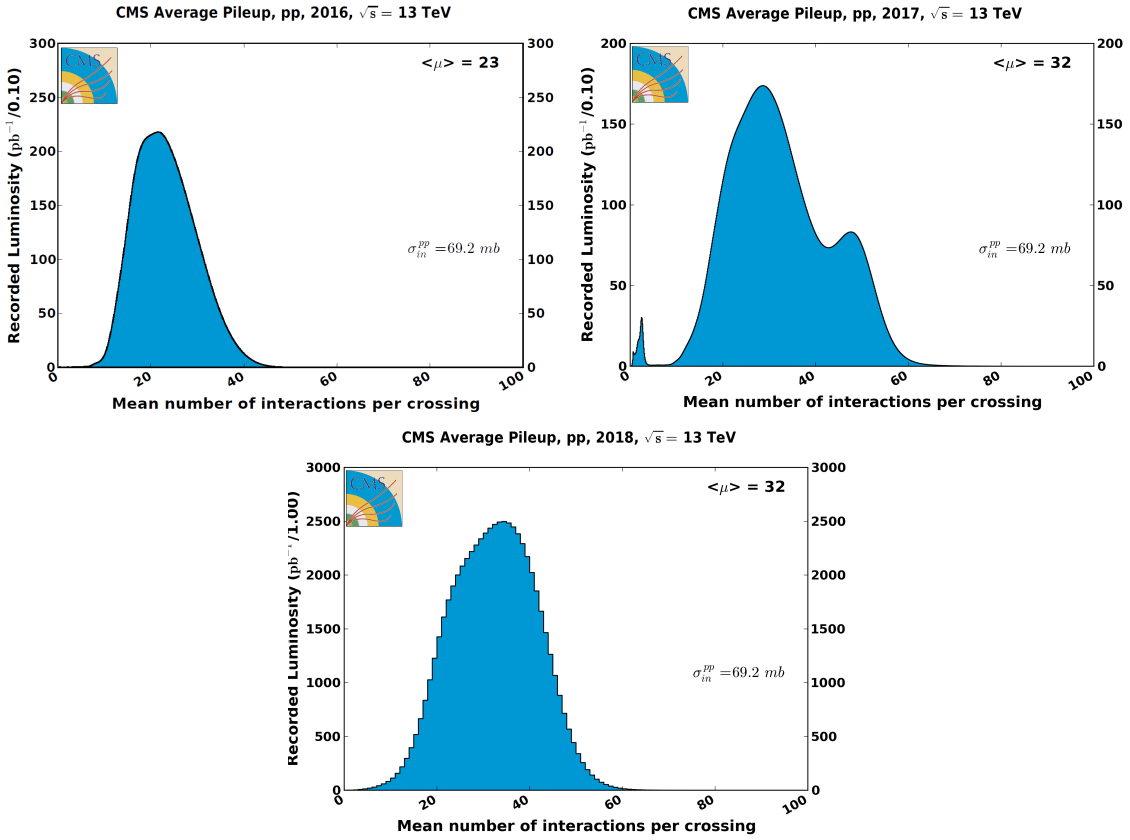

Figure 12: Average pile-up recorded in 2016 (top left), 2017 (top right) and 2018 (bottom) at CMS. Taken from [38].

4 Datasets and samples

The data used for this analysis was recorded by the CMS experiment in 2016, 2017 and 2018. The data is compared to simulated Monte Carlo signal and background samples. The signal needs to be distinguished from known standard model background processes with similar signatures.

4.1 Signal

The HVT signal samples are produced at leading order with two different production mechanisms, $q\bar{q}$ annihilation and vector boson fusion. The Z' resonance width is set to 0.1% of the resonance mass to fulfill the narrow-width approximation. The Z' is forced to decay to Higgs and Z bosons and the Z bosons to leptons and neutrinos. The Higgs bosons do not have any restrictions on the decay channel. The cross sections for the HVT model B and C are described in Table 1.

Z' mass (GeV)	$\sigma \times \mathcal{B}$ (pb) HVT model B	$\sigma \times \mathcal{B}$ (pb) HVT model C
800	0.855309 · 0.567236	3.352141e-3 · 0.500874
1000	0.509804 · 0.517614	1.094491e-3 · 0.496030
1200	0.271104 · 0.500699	4.226482e-4 · 0.495921
1400	0.146961 · 0.492143	1.819783e-4 · 0.492476
1600	0.0822156 · 0.487091	8.366986e-5 · 0.499822
1800	0.0473673 · 0.483825	4.172603e-5 · 0.492498
2000	0.0279823 · 0.481578	2.155255e-5 · 0.490429
2500	0.00815289 · 0.478265	4.678337e-6 · 0.490559
3000	0.00257265 · 0.47653	1.144028e-6 · 0.494481
3500	0.000850838 · 0.475504	3.064356e-7 · 0.491457
4000	0.000288261 · 0.474847	8.561628e-8 · 0.488809
4500	0.0000984981 · 0.4744	2.411154e-8 · 0.491466
5000	0.0000339139 · 0.474847	6.836269e-9 · 0.492081

Table 1: $Z' \to ZH$ production cross sections in HVT model B and C. The cross section for each relative sample is obtained by multiplying the production cross section by the vector boson branching fractions ($\mathcal{B}(Z \to \ell\ell) = 0.101$ and $\mathcal{B}(Z \to \nu\nu) = 0.200$ [39]).

4.2 Background samples

All physics processes with signatures similar to the signal (two leptons or large missing transverse momentum in association with a jet) have to be considered as background. The list of background samples are shown in Tables 2- 3 together with the cross sections used for normalization.

- **Z+jets**: The Z boson decays in 30% of the cases into a pair of charged leptons or neutrinos, making the Z+jets background the main irreducible background. In contrast to the signal, the p_T of the final state quarks of the Z+jets background have a softer spectrum and the di-jet mass distribution is non-resonant and rapidly falling. The Z+jets background is produced at leading order (LO) and normalized to the next-to-next-to-leading-order (NNLO) cross section. The V boson p_T spectra are corrected to account for next-to-leading-order (NLO) QCD and EWK and NNLO QCD contributions [40]. Figure 13 shows the scale factors used in the analysis. The samples are produced in bins of H_T (the sum of the p_T of the hadrons) starting from 100 GeV.

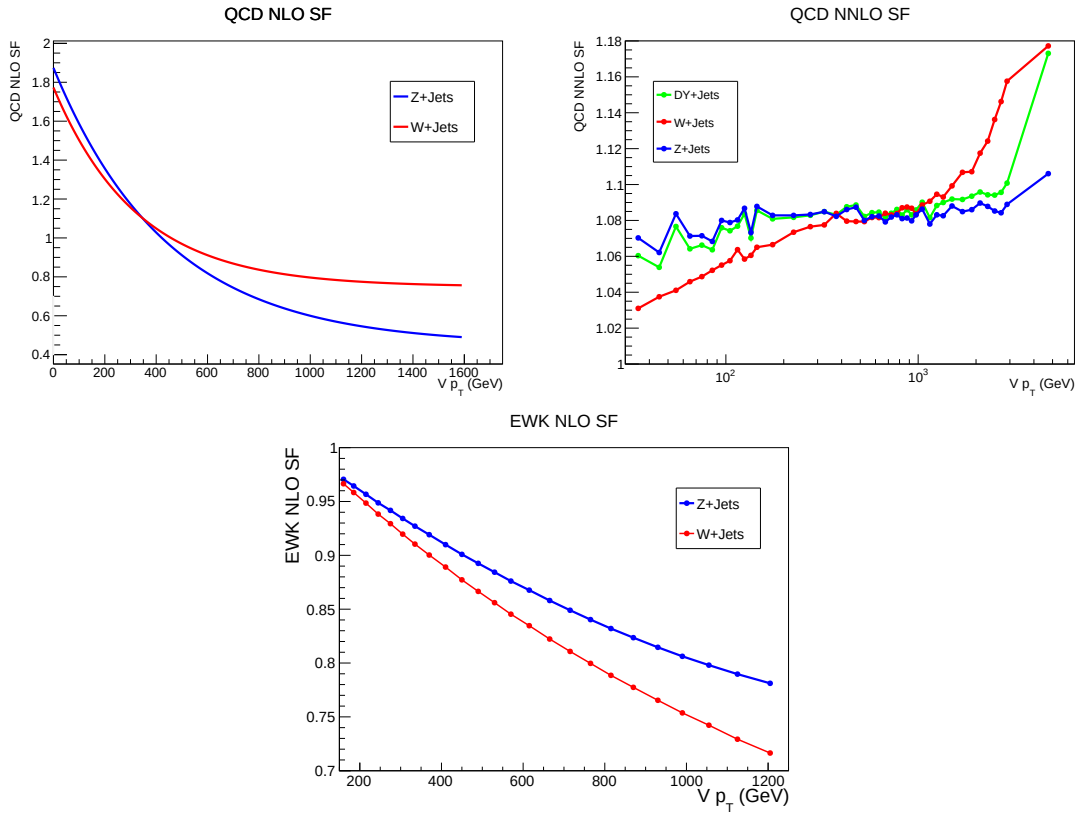

Figure 13: Scale factors for QCD NLO (top left), for QCD NNLO (top right) and for EWK NLO (bottom) [40].

- **W+jets**: The W boson decays leptonically into a charged lepton and a neutrino. If the charged lepton is not measured in the detector the W+jets background can be an irreducible background for the zero-lepton channel. The cross section of the W+jets background is an order of magnitude larger than the Z+jets background, therefore it has to be considered even if lepton veto is

applied. An inclusive $W \to \ell\nu$ sample has been produced at leading order in QCD in H_T-binned samples and normalized to NNLO inclusive. The same p_T-dependent QCD and EWK corrections as were used in the Z+jets background were applied.

- **$t\bar{t}$**: The $t\bar{t}$ pairs decay into two energetic b quarks and two W bosons, which can decay into isolated leptons and neutrinos. The $t\bar{t}$ background can be distinguished from the signal by its larger jet multiplicity and its broader distribution of the azimuthal angle between the vector boson and the dijet system. Because of the absence of the dilepton resonance in $t\bar{t}$ production, the dilepton p_T spectrum is rapidly falling, making the Z p_T cut important to reduce $t\bar{t}$ background in the dilepton channel. The main sample considered is generated at NLO in QCD and normalized to NNLO.

- **single top quark (S_T)**: Inclusive single-top-quark samples have been produced at NLO in QCD, including all the possible decays of the W bosons.

- **Diboson**: The production of two vector bosons is a rare process, but it has similar kinematics to the signal. The VV background can be reduced by applying a tight cut on the jet mass. The only way to distinguish a SM Higgs boson production associated with a vector boson (VH) background from the signal is by the heavy resonance mass, but the production cross section is much smaller than for the other VV processes. All diboson production processes (WW, WZ, ZZ, WH, ZH) are considered and simulated at NLO in QCD.

4.3 Data

The data samples used in this analysis were collected from 2016 to 2018 by the CMS experiment at a center-of-mass energy of 13 TeV. The data events have to pass the triggers associated to the respective dataset. The full list of datasets used is shown in Table 4 for 2016, in Table 5 for 2017 and Table 6 for 2018. The integrated luminosity L expresses the amount of recorded data and is shown in Fig. 14 for Run 2. The amount of data suitable for physical analysis is 35.9 fb^{-1}, 41.5 fb^{-1} and 59.97 fb^{-1} for data recorded in 2016, 2017 and 2018, respectively.

Dataset	$\sigma \times \mathcal{B}$ (pb)
DYJetsToLL_M-50_HT-100to200	147.4
DYJetsToLL_M-50_HT-200to400	40.99
DYJetsToLL_M-50_HT-400to600	5.678
DYJetsToLL_M-50_HT-600to800	1.367
DYJetsToLL_M-50_HT-800to1200	0.6304
DYJetsToLL_M-50_HT-1200to2500	0.1514
DYJetsToLL_M-50_HT-2500toInf	0.003565
ZJetsToNuNu_HT-100To200	280.35
ZJetsToNuNu_HT-200To400	77.67
ZJetsToNuNu_HT-400To600	10.73
ZJetsToNuNu_HT-600To800	2.559
ZJetsToNuNu_HT-800To1200	1.1796
ZJetsToNuNu_HT-1200To2500	0.28833
ZJetsToNuNu_HT-2500ToInf	0.006945
WJetsToLNu_HT-100To200	1345
WJetsToLNu_HT-200To400	359.7
WJetsToLNu_HT-400To600	48.91
WJetsToLNu_HT-600To800	12.05
WJetsToLNu_HT-800To1200	5.501
WJetsToLNu_HT-1200To2500	1.329
WJetsToLNu_HT-2500ToInf	0.03216

Table 2: Z, W +jets simulated samples. The cross section $\times$ branching ratio is shown in pb. SM boson branching fractions are taken from Ref. [39].

Dataset	$\sigma \times \mathcal{B}$ (pb)
TTTo2L2Nu	87.31
TTToSemiLeptonic	364.35
TTWJetsToLNu	0.2043
TTZToLLNuNu	0.2529
ST_s-channel_4f_leptonDecays	3.36
ST_t-channel_top_4f_InclusiveDecays	136.02
ST_t-channel_antitop_4f_InclusiveDecays	80.95
ST_tW_top_5f_inclusiveDecays	35.85
ST_tW_antitop_5f_inclusiveDecays	35.85
WWTo1L1Nu2Q	49.997
WWTo2L2Nu	12.178
WWTo4Q	51.723
WZTo2L2Q	5.595
ZZTo2Q2Nu	4.04
ZZTo2L2Q	3.22
ZZTo2L2Nu	0.564
ZZTo4L	1.212
GluGluHToBB_M125	$43.92 \cdot 0.5824$
ZH_HToBB_ZToNuNu_M125	$0.7612 \cdot 0.5824 \cdot 0.201$
ZH_HToBB_ZToLL_M125	$0.7612 \cdot 0.5824 \cdot 0.1097$
WplusH_HToBB_WToLNu_M125	$0.84 \cdot 0.5824 \cdot 0.1085$
WminusH_HToBB_WToLNu_M125	$0.533 \cdot 0.5824 \cdot 0.1085$

Table 3: $t\bar{t}$, dibosons and multijet simulated samples. The cross section $\times$ branching ratio is shown in pb. SM boson branching fractions are taken from Ref. [39].

Dataset
MET/Run2016B-H
SingleMuon/Run2016B-H
SingleElectron/Run2016B-H

Table 4: 2016 Datasets with an integrated luminosity of 36.8 fb^{-1}.

Dataset
MET/Run2017B-F
SingleMuon/Run2017B-F
SingleElectron/Run2017B-F

Table 5: 2017 Datasets with an integrated luminosity of 41.7 fb^{-1}.

Dataset
MET/Run2018A-D
SingleMuon/Run2018A-D
EGamma/Run2018A-D

Table 6: 2018 Datasets with an integrated luminosity of 59.9 fb^{-1}.

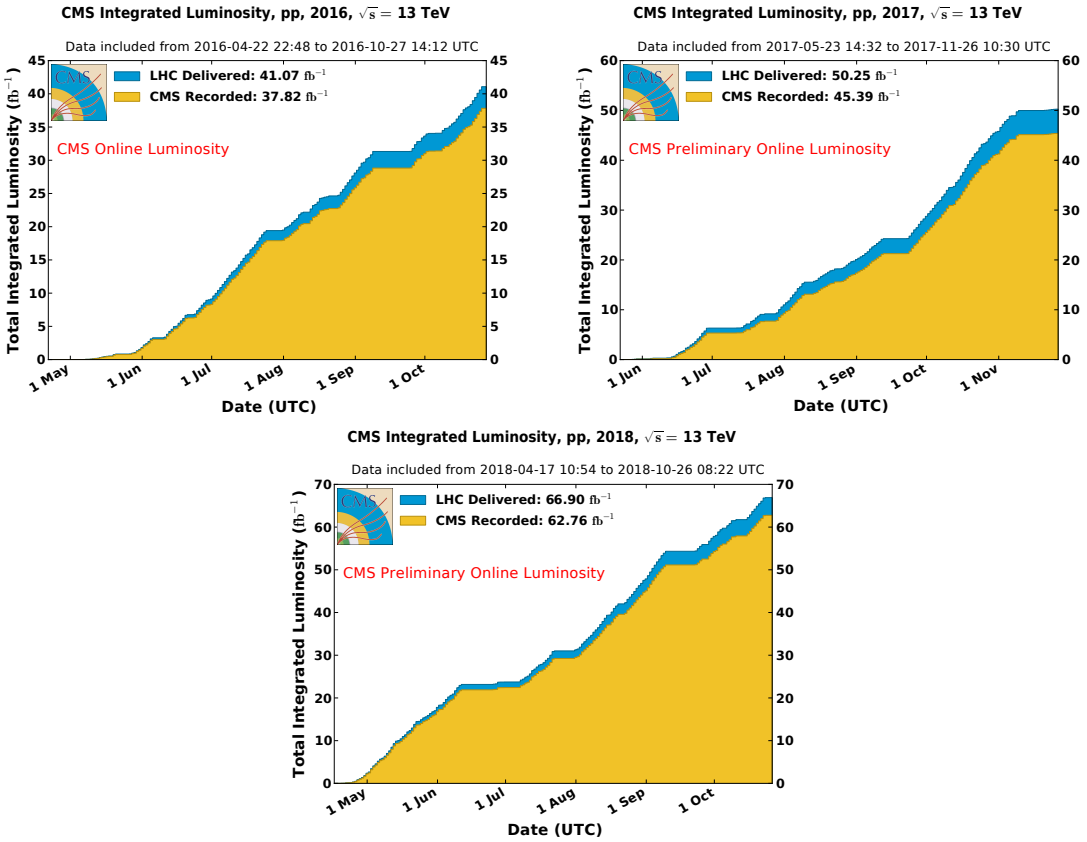

Figure 14: Cumulative luminosity versus day delivered to (blue), and recorded by CMS (orange) during stable beams and for pp collisions at 13 TeV centre-of-mass energy in 2016 (top left), 2017 (top right), 2018 (bottom). Retrieved from [38].

5 Event reconstruction

This section describes how physics objects are reconstructed based on their signature in the different subdetectors as shown in Fig.15. Only particles with a sufficient lifetime can be detected, the others need to be reconstructed from their decay particles. Hadrons, especially quarks and gluons, decay into a spray of particles called a jet. Charged particles ionize the silicon semiconductors of the tracker and leave a curved track due to the Lorentz force. The transverse momentum of the particle can be obtained from the curvature of the track, the more curved the track, the smaller its transverse momentum. Neutral particles like photons are not affected by the magnetic field and leave no track. Electrons and photons deposit their energy by inducing an electromagnetic shower in the electromagnetic calorimeter. Hadrons interact via the strong interaction and may induce a hadronic shower in the electromagnetic calorimeter, which is fully absorbed in the hadronic calorimeter. The muons are barely interacting with the calorimeters due to their large mass and are detected in the muon chambers. Neutrinos cannot be detected in the CMS detector and are identified as an imbalance in the transverse energy of all measured particles.

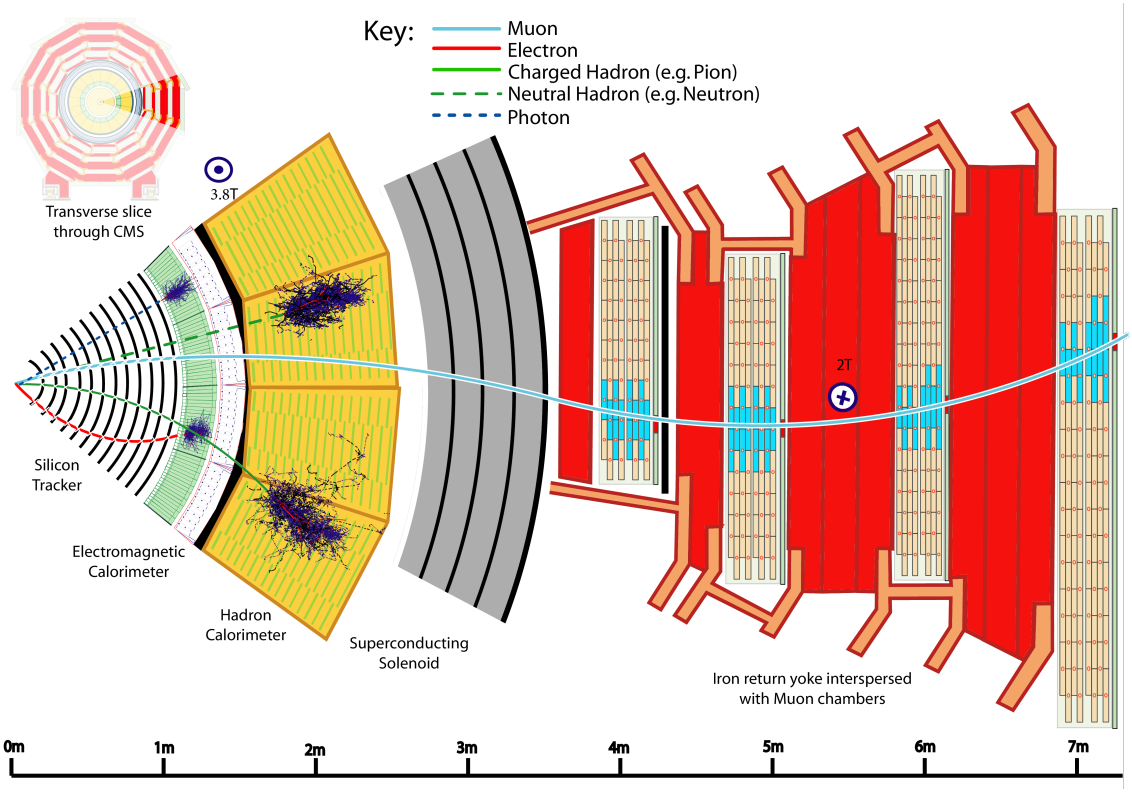

Figure 15: Illustration of the subdetectors with interactions of different particles. Taken from [41].

5.1 Particle Flow

Particles are reconstructed and identified using the particle-flow (PF) algorithm [41], which links the reconstructed tracks in the tracker to the energy deposits in the calorimeters and muon chambers. Muons are first identified by extrapolating the tracks to the calorimeters and muon chambers and linking clusters to the track if the extrapolated position lies within the cluster area. The electrons are identified by linking the tracks to the clusters in the electromagnetic calorimeter. Photon clusters are linked to the electron track to account for the frequent Bremsstrahlung photon emission. Isolated photons are identified in the same step. The tracks and clusters associated to muons, electrons and isolated photons are removed from consideration for the next steps. Tracks are linked to clusters in the hadronic calorimeter for the identification of hadrons. The remaining clusters in the electromagnetic and hadronic calorimeter are associated to photons and neutral hadrons, respectively. The identified particles, containing neutral and charged hadrons, photons, electrons and muons, are then used to reconstruct jets, missing transverse energy and identify taus from their decay products.

5.2 Trigger

Data events are only recorded if they satisfy trigger requirements, therefore, the trigger is also simulated on Monte Carlo events. The efficiency of the triggers can be different in data than in Monte Carlo, causing a discrepancy. In order to correct for any potential discrepancies, scale factors are applied to simulated events. The scale factors are defined as $SF = \varepsilon_{\text{data}}/\varepsilon_{MC}$, with $\varepsilon_{\text{data}}$ being the efficiency in data and ε_{MC} the efficiency in Monte Carlo. For the di-lepton channels we use a single-lepton trigger, which requires at least one, non-isolated lepton. We assume that the higher p_T lepton fires the trigger. For the zero-lepton channel a set of E_T^{miss} triggers are used, which require missing transverse momentum.

5.2.1 Electron triggers

Electrons are selected using triggers that require a single isolated electron with $p_T > 35$ GeV or a non-isolated electron with $p_T > 115$ GeV to ensure an optimal efficiency over the whole p_T range. The single-electron trigger efficiencies are derived using a tag and probe method on $Z \to \ell\ell$ events. The electron trigger scale factors are applied to all Monte Carlo samples.

5.2.2 Muon triggers

Muons are selected with triggers requiring a single non-isolated global muon with $p_T > 50$ GeV or a tracker muon with $p_T > 100$ GeV, because the $Z \to \mu\mu$ events are very boosted, the muons are typically close to each other. Global muon refers to the muons reconstructed in the tracker and the muon chambers, tracker muons are only reconstructed from tracker information. The efficiencies of the single muon triggers are derived with a tag and probe procedure by selecting $Z \to \ell\ell$ events. The trigger

efficiency is evaluated by selecting the *probes* by a tight-lepton identification and studying the tagged lepton efficiency as a function of p_T and η for data and Monte Carlo. The trigger scale factors are applied to simulated events to match the trigger efficiency measured in data.

5.2.3 Missing energy triggers

Events with $Z \to \nu\nu$ are identified with a set of triggers requiring a E_T^{miss}, calculated with or without considering muons, or a hadronic missing transverse energy (MHT) of larger than 110 GeV. The efficiency of the 2016 E_T^{miss} triggers is measured by selecting $W \to e\nu$ events in the Single Electron dataset, which fire the E_T^{miss} triggers. The events need to have one electron with $p_T > 30$ GeV, $|\eta| < 2.1$, passing tight identification and isolation requirements, and with a minimum separation in the azimuthal angle $\Delta\phi(e, E_T^{miss}) > 0.5$. These events account for the denominator. The numerator is represented with events required to fire at least one of the E_T^{miss} triggers. Figures 16 and 17 show the trigger efficiency for 2016 and 2017/2018. The efficiency of the trigger is almost 1 for E_T^{miss} above the threshold, therefore the value was fixed at 1.

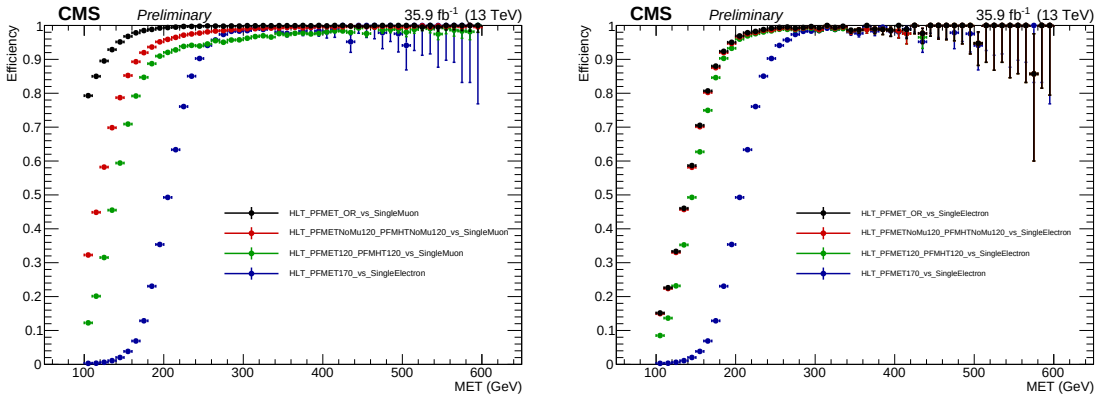

Figure 16: Trigger efficiency for the E_T^{miss} triggers used for 2016 as function of the minimum value between the offline reconstructed E_T^{miss} and $H_{\mathrm{T}}^{\mathrm{miss}}$. The efficiencies are calculated from the SingleElectron (left) and SingleMuon (right) dataset.

5.3 Vertex and Pile-up

Several vertices are reconstructed per bunch crossing. The primary vertex is chosen as the one with the highest sum of p_T^2 of all reconstructed particles and missing transverse momentum [44] and has to fulfill the following conditions:

- number of associated tracks > 0
- number of degrees of freedom $N_{DoF} > 4$
- vertex position along the beampipe $|z_{vtx}| < 24$ cm
- vertex distance with respect the beam pipe $d_0 < 2$ cm

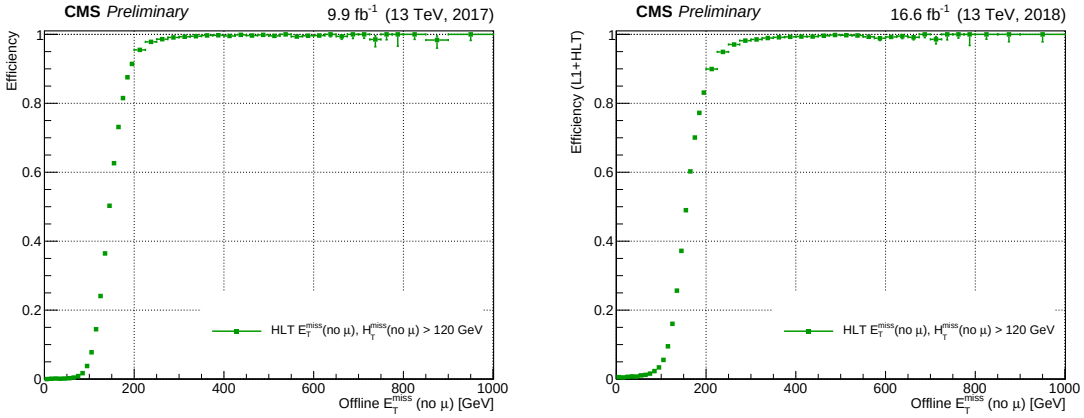

Figure 17: The 2017 (left) and 2018 (right) E_T^{miss} Trigger efficiency as a function of the offline reconstructed E_T^{miss}. The efficiences are calculated from the SingleMuon dataset [42][43].

where z_{vtx} and d_0 are the distance along and perpendicular to the beam line of the vertex with respect the nominal interaction point $(0, 0, 0)$.

All reconstructed tracks not originating from the primary vertex are caused by pileup. The pileup Monte Carlo distribution needs to be reweighted to match the pileup distribution in data. The standard CMS PU reweighting technique [45, 46] is used, assuming a total inelastic cross section of $\sigma_{in} = 69.2$ mb.

5.4 Electrons

Electrons are reconstructed by matching energy deposits in the fiducial pseudorapidity range of the electromagnetic calorimeter ($|\eta| < 2.5$) to tracks reconstructed in the silicon tracker. Tracks are reconstructed using Gaussian sum filters to model and fit the energy loss of the electrons. The electrons are identified taking the energy deposited along the electron trajectory, the direction and momentum of the track and its compatibility with the primary vertex into account [47]. Electrons are required to pass an isolation requirement, defined as the sum of transverse momenta of all particles within $\Delta R = \sqrt{(\Delta\eta)^2 + (\Delta\phi)^2} = 0.3$ around the electron track, after the contribution from the electron itself, other nearby electrons, and pileup is removed. The electron identification is described in more detail in Ref.[48].

The selection efficiency has to be tested with very boosted events, where two electrons are close to each other. The selection efficiency as a function of ΔR and p_T of the two electrons is shown in Fig. 18.

Scale factors are applied to the simulated events to cover any differences in the electron identification efficiency between Monte Carlo and data. They are derived with a tag-and-probe method on the $Z \to ee$ mass peak as a function of p_T and η of the electrons.

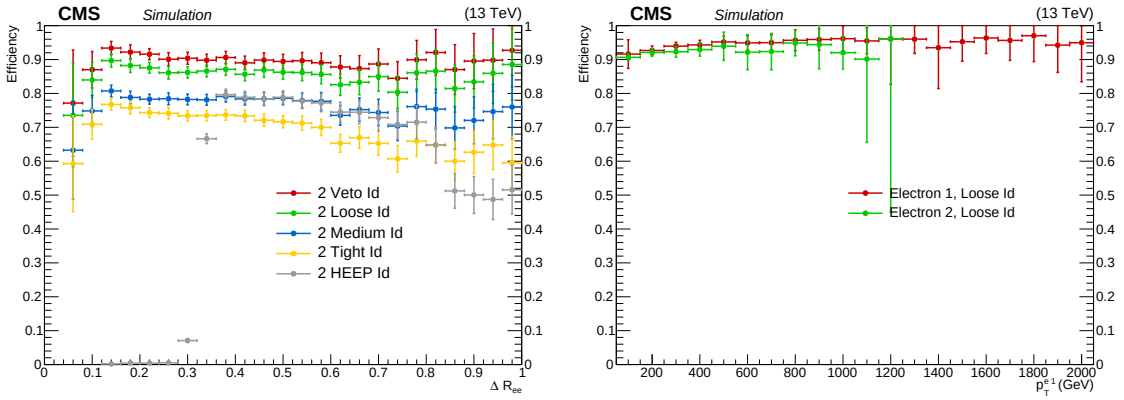

Figure 18: Electron identification efficiency as a function of the ΔR between the two electrons at generation level (left) and p_T (right), after matching and p_T selections. Events from different signal samples are considered together.

5.5 Muons

Muons are reconstructed within the acceptance of $|\eta| < 2.4$ by matching tracks in the silicon tracker and energy deposits in the muon chambers. The compatibility of the tracks to the primary vertex is also taken into account. Muon candidates are identified either using only the tracker information (tracker muons) or the reconstructed tracks from the tracker and energy deposits in the muon detector (global muons). The global muon reconstruction drops for small separation ΔR between the muons. For this reason at least one muon has to be identified as a global muon and the other as a tracker muon. Muons are required to be isolated by imposing a limit on the sum of transverse momenta of reconstructed tracks within a cone $\Delta R = 0.3$ around the muon track, not including the muon itself and tracks attributed to other muons. The muon indentification is discussed in Ref. [49].

The muon selection efficiency is derived in the same way as for the electrons and shown in Figure 19 as function of ΔR between the muons, proving the applied approach prevents a loss of efficiency at low ΔR.

Scale factors for the muon track reconstruction, identification and isolation are used as a function of muon p_T and η, and are applied to all simulated events [50].

5.6 Taus

Taus are selected if $p_T > 180$ GeV, $|\eta| < 2.3$ and $\Delta R > 0.4$ from other isolated electrons and muons. They are used as a veto in the signal and control regions. The identification of taus is described in detail in Ref.[51].

5.7 Jets

For the analysis jets with a cone size of $R = 0.4$ (AK4 jets) and of $R = 0.8$ (AK8 jets) are used. For the removal of pileup contributions two different methods are

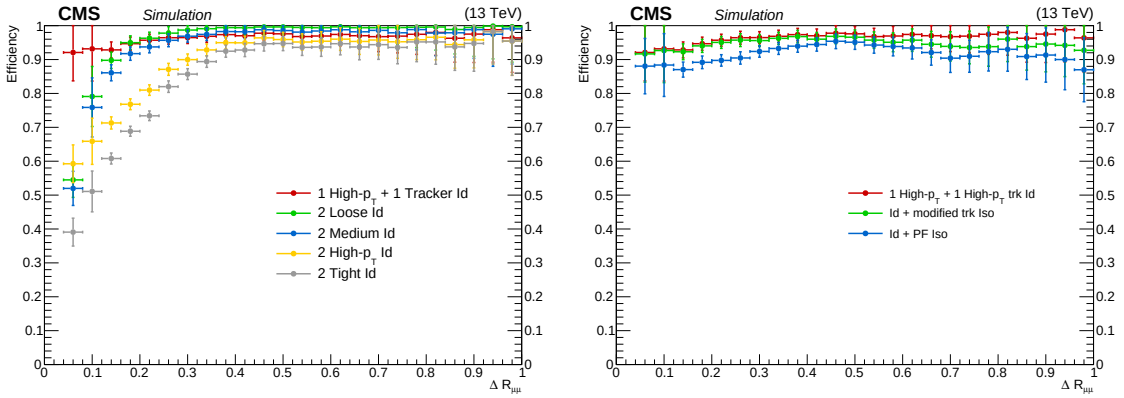

Figure 19: Identification (left) and combined identification and isolation (right) efficiency as a function of the ΔR at generation level, after matching and p_T selections, when muons are required to pass different identification and isolation requirements. Events from all the generated mass points are considered together.

applied. The charged hadron subtraction algorithm (CHS) [52] is used for AK4 jets and the pileup per particle identification (PUPPI) [53] for AK8 jets. CHS removes charged hadrons not originating from the primary vertex and PUPPI computes a weight for every particle, measuring how pileup-like a particle is. After the pileup contributions are removed, the remaining particles are clustered using the FastJet package [54] with the anti-k_T jet clustering algorithm [55]. The selection criteria for AK4 jets is p_T larger than 30 GeV, $|\eta| < 2.4$ and $\Delta R > 0.4$ afar from isolated leptons. The AK8 jets need a p_T larger than 200 GeV and $|\eta| < 2.4$.

5.7.1 Jet mass

The Jet mass is important as it is used to distinguish a Higgs-boson jet from a QCD jet. The rate of QCD jets with a mass around the Higgs boson mass can be reduced by applying a grooming algorithm, which removes soft and large-angle radiation originating from pileup. This procedure lowers the jet mass of QCD jets but maintains the jet mass of Higgs-boson jets. The used algorithm is called *Soft Drop* and recursively removes soft wide-angle radiation from the jet [56]. *Soft Drop* is applied on the PUPPI AK8 jet.

5.8 Bottom quark identification

The b quarks have a relatively long lifetime of 10^{-12} s, producing a secondary vertex as shown in Figure 20. An important measure for finding a secondary vertex is the impact parameter, which is the distance from the track's closest point to the primary vertex. An algorithm using the secondary vertex and track parameters can be used to identify jets originating from b quarks. The secondary vertices are reconstructed with the inclusive vertex finder algorithm [57]. The secondary vertex reconstruction efficiency is 50 $\sim$ 60%, therefore also tracks where no vertex could be found are used. To do this, tracks having an impact parameter significance (d_0/σ) of larger

than 2 are combined to a pseudo vertex, with all other tracks being considered in a no-vertex category. The vertex information together with track information are fed as inputs to an Artificial Neural Network. The output of the neural network is a discriminator value stating how likely a jet is to originate from a b-quark. A jet is considered as b-tagged if the discriminator value is above a threshold value, called a working point.

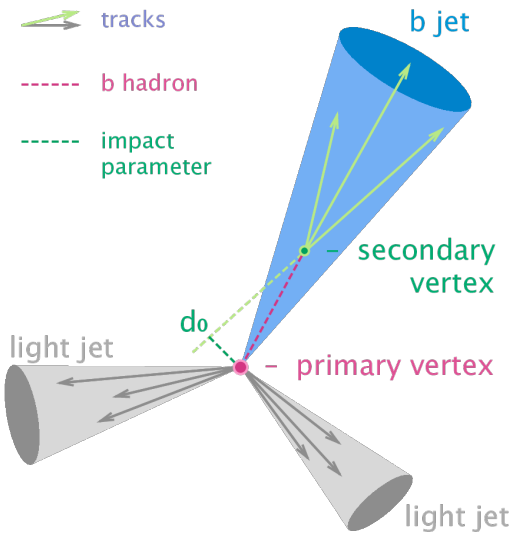

Figure 20: Bottom quark identification. Taken from [58].

5.8.1 Subjet DeepCSV

The algorithm used for this analysis is DeepCSV. It is based on the pfCombinedInclusiveSecondaryVertexV2BJetTags, or *combined secondary vertex (CSV)* for short, and also includes the additional charged particle tracks. Three working points are defined for each year and reported in Tables 7, 8 and 9. The looser the cut the larger the b-tagging efficiency but also the larger the mis-tag rate. In this analysis the loose working points are applied for all years. The b-tagging is applied to the subjets of the AK8 jet.

Working point	Cut	ε_{light}
Loose	0.2217	$\sim 10\%$
Medium	0.6321	$\sim 1\%$
Tight	0.8953	$\sim 0.1\%$

Table 7: 2016 DeepCSV official working points.

To account for a difference in the b-tagging efficiency for data and Monte Carlo, scale factors are applied to simulated events. The DeepCSV scale factors are provided for b-jets and mistagged light jets and the three working points [59]. A weight is calculated per-event using the b-tag value and the flavour of the hadron which initiated the jet. An average systematic uncertainty of 6% per b jet, 12% per c

Working point	Cut	ε_{light}
Loose	0.1522	$\sim 10\%$
Medium	0.4941	$\sim 1\%$
Tight	0.8001	$\sim 0.1\%$

Table 8: 2017 DeepCSV official working points.

Working point	Cut	ε_{light}
Loose	0.1241	$\sim 10\%$
Medium	0.4184	$\sim 1\%$
Tight	0.7527	$\sim 0.1\%$

Table 9: 2018 DeepCSV official working points.

jet, and 15% per light quark and gluon jet is used to account for the normalization uncertainty [60].

5.8.2 Choice of the b-tagging algorithm

The performance of the b-tagging algorithms can be compared using ROC curves, which are derived using the b-tagging efficiency for Higgs bosons and the mis-tagging efficiency for non-Higgs bosons using simulation, and information from the generator level. Tags are considered as AK8 jets from signal events, and mistags are considered from AK8 jets from SM background processes. The events need to pass the selection used in the analysis including the jet-mass cut. The ROC curves are shown in Fig. 21 for CSV, DeepCSV, double-b-tagger and DeepTagMD taggers. CVS1 and DeepCSV1 correspond to the maximal tagger value of both sub-jets, CSV2 and DeepCSV2 to the minimal value. CSV shows the mean of CSV1 and CSV2, DeepCSV the mean of DeepCSV1 and DeepCSV2. Even though DeepTagMD_ZHbbvsQCD would show the best performance it is not chosen due to the mass sculpting effect. Instead DeepCSV is used in this analysis.

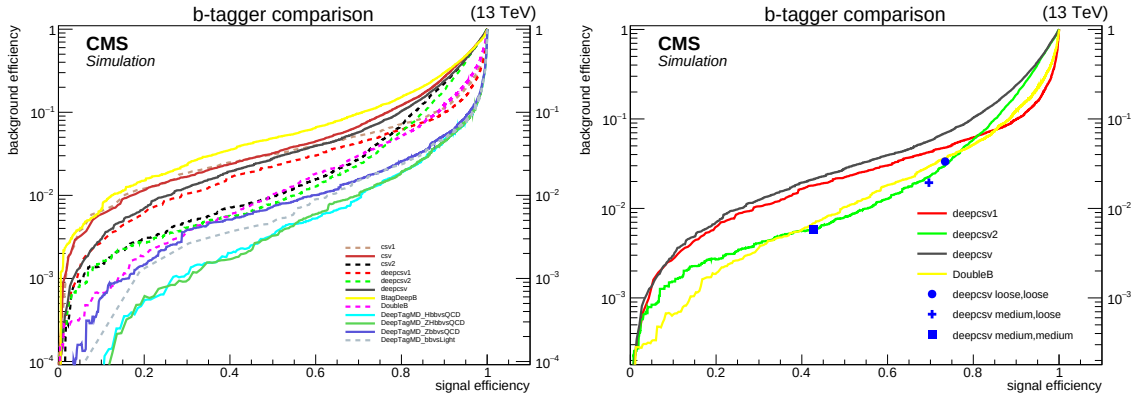

Figure 21: Left: ROC curves for the considered b-tagging algorithms. Right: ROC curves with markers for loose, medium and tight working points of DeepCSV.

A mass-sculpting effect describes a change in jet-mass distribution caused by the

tagger, which could lead to a bump in the signal region. This is dangerous, as this bump could be mistaken as a signal. A tagger can be tested for a mass-sculpting effect by comparing the normalized sum of the jet mass distribution with different tagger cuts applied. This is shown in Figure 22 for a combined sample. In order to have a similar efficiency for both taggers, the range of the cuts are different. The tagger DeepTagMD_ZHbbvsQCD shows a large mass-sculpting effect, therefore DeepCSV was chosen.

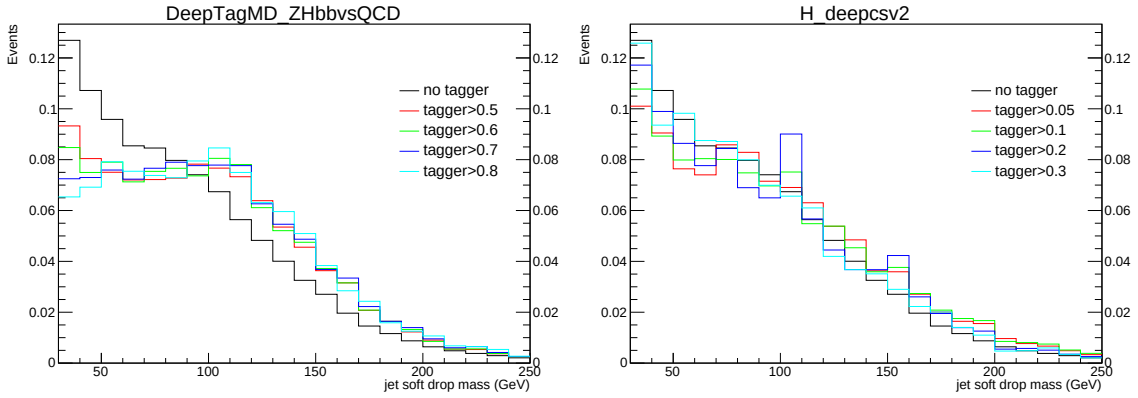

Figure 22: Mass sculpting effect for the taggers DeepTagMD_ZHbbvsQCD (left) and DeepCSV (right).

5.9 Missing Energy

The neutrinos cannot be measured in the detector, therefore they are described by the missing transverse energy, which is the imbalance in the transverse energy of all visible particles and derived with the particle flow algorithm [61]. The raw E_T^{miss} can be calculated from the inverse vectorial sum of the transverse momentum of all reconstructed particles by particle flow: $\vec{E_T^{miss}} = -\sum_{i=0}^{all} \vec{p_{T\,i}}$. Due to detector misalignment and the non-compensating nature of the calorimeters, the raw E_T^{miss} is different from the true E_T^{miss}. Jet energy corrections are propagated to the PUPPI E_T^{miss} to better estimate the true E_T^{miss}.

5.10 Vector boson fusion

The heavy resonance is accompanied by two high-p_T jets in vector-boson-fusion (VBF) production. The VBF production tag is derived by looking for jets which satisfy $|\eta| < 5$ and have a separation to the Higgs boson candidate and to isolated leptons of $\Delta R(H, jet) > 1.2$ and $\Delta R(\ell, jet) > 0.4$, respectively. The two jets with the largest transverse momentum must have opposite η, an η separation of larger than 4 ($\Delta\eta(jet_1, jet_2) > 4$) and a di-jet mass of larger than 500 GeV.

6 Boson recontruction

6.1 Z boson to neutrinos

In the zero-lepton channel the Z boson decays into a pair of neutrinos, which are not visible in the detector. Therefore the transverse mass of the heavy resonance is used. It uses the jet and E_T^{miss} kinematics and can be derived as follows:

$$m_{\nu\nu bb}^T = \sqrt{2E_T^j E_T^{miss} \cdot (1 - \cos\Delta\varphi(j, E_T^{miss}))}$$

6.2 Z boson to leptons

In the leptonic channels the Z boson can be reconstructed by a pair of leptons of same flavour, opposite charge and with the highest combined p_T in the event. The dilepton invariant mass is required to be between 70 and 110 GeV, and the transverse momentum of the dilepton system to be larger than 200 GeV.

6.3 Higgs boson reconstruction

The Higgs-boson candidate jet (j_H) is chosen as the leading-p_T AK8 jet with p_T larger than 200 GeV, $|\eta| < 2.4$ and not overlapping with isolated leptons by requiring $\Delta R(j_H, \ell) > 0.8$. The two variables used for Higgs-boson identification are the jet mass and the b-tagging. The invariant mass of all decay particles should be around the mass of the original particle. QCD jets, which are produced from quarks and gluons, typically have a smaller invariant mass. Therefore, the Higgs boson candidate is required to have a groomed jet mass compatible with the Higgs boson mass ($105 \leq$ soft drop PUPPI corrected mass ≤ 135 GeV). The jet mass is derived after applying **Soft drop** for grooming together with **PUPPI** to remove pileup contributions. For the kinematic selections of the AK8 jet and for the reconstruction of the heavy resonance mass the four momentum of the AK8 PUPPI jet is used. The Higgs boson decaying to a pair of b quarks and the inclusive decay channel, which includes all the other decay channels, are considered. The b-tagging requirement is applied to the particle flow CHF subjets. The Higgs-boson candidate jet can have either 0, 1 or 2 subjets, which pass the b-tagging selection. If both subjets are b-tagged the Higgs boson candidate is assigned to the 2 b-tagging category, otherwise to the $\leq$1 b-tagging category.

7 Event selection

The events have to pass a selection depending on the channel to be considered as signal candidates, both in data and simulation.

7.1 Neutrino channel

In the 0ℓ channel a E_T^{miss} larger than 250 GeV is required to account for the neutrinos, which cannot be measured in the detector. Data is collected using trigger selections described in section 5.2.3. Multijet production is suppressed by requiring that the minimal azimuthal angular separation between all AK4 jets and the missing transverse momentum vector satisfies $\Delta\phi(jet, E_T^{miss}) > 0.5$, and an azimuthal angular separation of $\Delta\phi(j_H, E_T^{miss}) > 2$. Events arising from detector noise are removed by requiring the contribution of the charged hadronic particles to the Higgs boson momentum be larger than 0.1, and the ratio E_T^{miss}/p_T^H to be larger than 0.6. Events with isolated leptons with $p_T > 10$ GeV or hadronically decaying τ leptons with $p_T > 18$ GeV are removed in order to reduce the contribution from other SM processes. The $t\bar{t}$ contribution is reduced by removing events with an additional b-tagged AK4 jet not overlapping with j_H. In the VBF category a $|\eta_{jH}| < 1.1$ is applied on the Higgs boson candidate to reject events where the Z and H bosons are emitted at large pseudorapidities, resulting in a significant underestimation of m_{T}^X.

7.2 Di-lepton channel

In the 2ℓ channel, data is collected using the electron and muon triggers described in section 5.2.1 and 5.2.2, respectively. The electrons are identified as described in section 5.4 and the muons as described in section 5.5. The leptons are required to have $p_T > 55$ and $p_T > 20$ GeV for the leading and subleading lepton, respectively. The di-lepton system is required to have a mass between 70 and 110 GeV and $p_T > 200$ GeV. The Z+jets background is reduced by requiring a separation between the Z boson candidate and j_H of $\Delta R(j_H, Z) > 2$ and additionally $|\Delta\eta(j_H, Z)| < 1.7$ in the non-VBF categories.

A sufficiently large Lorentz boost of the Higgs boson is ensured by requiring m_X to be larger than 750 GeV for all except the $\leq$1 b-tagging, non-VBF categories, where a higher cut at 1200 GeV is necessary to ensure the smoothness of the background model. A summary of the selections is given in Table 10.

The signal acceptance $\times$ efficiency is shown in Fig. 23 for the non-VBF signals and in Fig. 24 for the VBF signals, either with $Z \to \nu\nu$ or $Z \to \ell\ell$. The 0ℓ channels show the best signal efficiency. The signal efficiency of the 2 b-tagging categories decrease with $m_{Z'}$ because the subjets get collimated at high p_T, resulting in a lower track reconstruction and jet reconstruction efficiency.

	$Z \to ee$	$Z \to \mu\mu$	$Z \to \nu\nu$
Trigger	`HLT_Ele(115)`	`HLT_Mu50`	`HLT_PFMET`
	`HLT_Ele(35)`	`HLT_TkMu100`	or `HLT_PFMETNoMu`
	or `HLT_Pho(200)`	-	-
Lept Id	$2e$ *loose* WP	1μ HighPt, 1μ tracker HighPt	e, μ, τ veto
Lept Iso	inc. in Id	$tkIso < 0.1$	-
Lept p_T	$p_T > 55, 20$ GeV	$p_T > 55, 20$ GeV	-
Z boson p_T	$p_T^V > 200$ GeV		$E_T^{miss} > 250$ GeV
Z boson mass	$70 < m_{\ell\ell} < 110$ GeV		-
H-jet	AK8 PFJet, $p_T > 200$ GeV		
H mass	$105 < m_j < 135$ GeV (SR), $30 < m_j < 65$ GeV, $m_j > 135$ GeV (SB)		
H b-tag	$\leq$1 or 2 subjets b-tagged *loose*		
heavy resonance mass	$m_T^X > 750$ GeV	$m_X > 750$ GeV	
top quark rejection	-	-	veto max b-tag *loose* AK4 jets
QCD rejection	-	-	min $\Delta\varphi_{jets,E_T^{miss}} > 0.5$
Noise cleaning	-	-	$\Delta\varphi_{j_H,E_T^{miss}} > 2$
	$\lvert\Delta\eta(Z, j_H)\rvert < 1.7$		-
Separation	$\Delta R_{j_H - Z} > 2$		-
MET Correction	-	-	chf > 0.1, $MET/H_{p_T} > 0.6$

Table 10: Summary of the selection criteria.

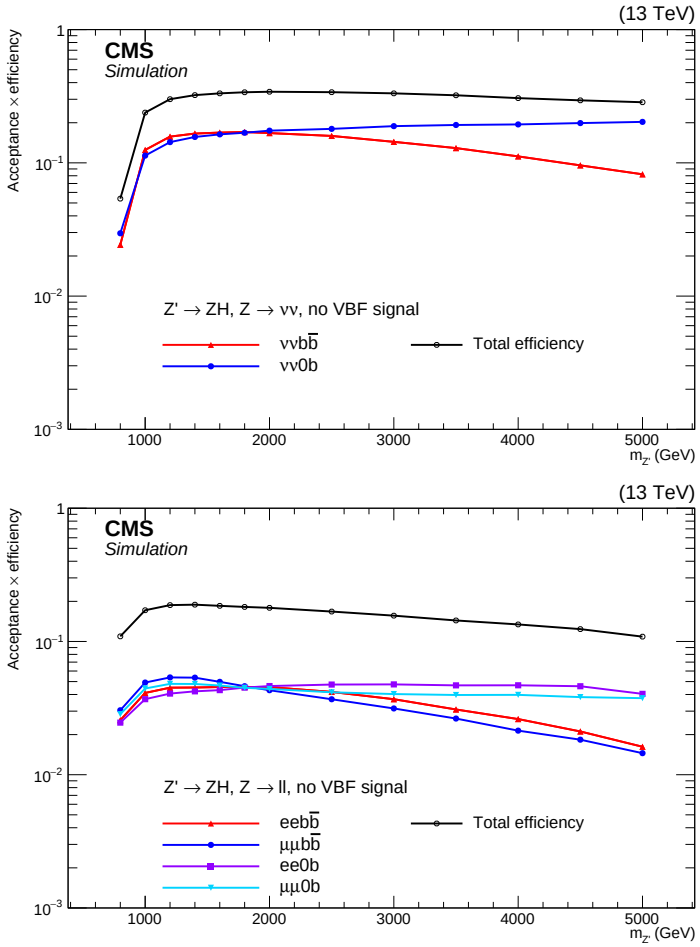

Figure 23: Signal acceptance $\times$ efficiency in 0ℓ (top) and 2ℓ (bottom) categories. The signal is produced through $q\bar{q}$ annihilation.

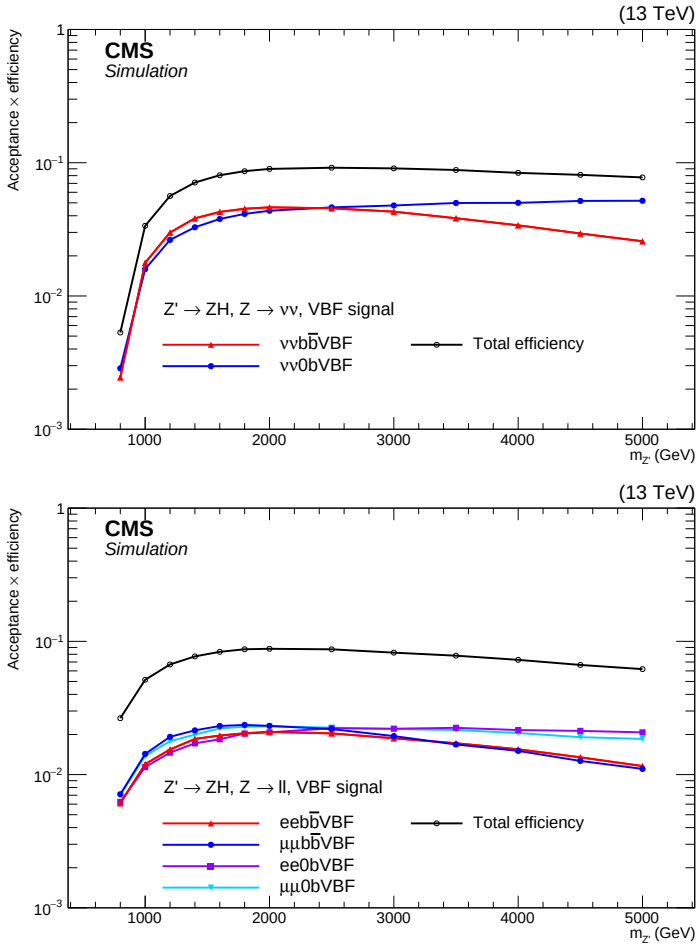

Figure 24: Signal acceptance × efficiency in 0ℓ (top) and 2ℓ (bottom) categories. The signal is produced through vector boson fusion.

8 Top-quark control regions

The top-quark contribution ($t\bar{t}$ and single-top-quark) is taken directly from simulation for the alpha method, therefore it needs to be validated on data. For this reason top-quark scale factors are derived using top-quark control regions (CR), selecting an almost pure $t\bar{t}$ sample.
The 0ℓ top-quark control region uses the selections described in section 7, but removes the b-tag veto on other AK4 jets and adds the requirement for one additional AK4 jet, b-tagged with the *tight* working point.
For the 2ℓ top-quark control regions one muon and one electron of opposite charge are required. The lepton identification stays the same, but both leptons need to have a p_T of larger than 30 GeV, a combined p_T of larger than 120 GeV and a dijet mass of larger than 110 GeV. The scale factors for b-tagging and lepton identification are applied.
In the 0ℓ top-quark control region the estimation of the top-quark scale factors could be biased due to a significant contribution from V+jets background. For this reason an intermediate control region requiring a AK4 jet with a b-tag value between the *medium* and the *tight* working point is used to perform a rescaling of the V+jets background. The formula for deriving the scale factor with m being the medium-tight and t the tight region is:

$$SF_{top} = \frac{N_t^D - N_m^D \frac{N_t^V}{N_m^V}}{N_t^T - N_m^T \frac{N_t^V}{N_m^V}}$$

where N^D, N^V, and N^T are the number of events in data, V+jets, top-quark samples, respectively. The uncertainties are propagated with the same formula, considering the dominant statistical uncertainty. In the 2ℓ channel the top-quark scale factors are evaluated using only the control region due to small V+jets contribution.

In Figures 25 and 26 the data and simulation is shown for the top-quark control region for the 0ℓ and 2ℓ non-VBF categories. The top-quark scale factors are derived separately for each category and applied in the alpha background prediction method. The limited number of data introduces a statistical uncertainty to the top-quark scale factors. Systematic uncertainties in the lepton identification and the b-tagging lead to a systematic uncertainty of the top-quark scale factor, which is further described in sec. 11. The VBF categories have a normalization uncertainty applied to account for the small statistics in these control regions.

non-VBF category		Top-quark SF ± stat. ± syst.
2 b-tag	0ℓ	$1.012 \pm 0.116 \pm 0.008$
	$1e, 1\mu$	$1.098 \pm 0.084 \pm 0.001$
	$2e$	$1.098 \pm 0.084 \pm 0.067$
	2μ	$1.098 \pm 0.084 \pm 0.075$
$\leq$1 b-tag	0ℓ	$1.028 \pm 0.048 \pm 0.009$
	$1e, 1\mu$	$1.003 \pm 0.021 \pm 0.005$
	$2e$	$1.003 \pm 0.021 \pm 0.089$
	2μ	$1.003 \pm 0.021 \pm 0.095$
VBF category		Top-quark SF ± stat. ± syst. ± VBF norm
2 b-tag	0ℓ	$0.676 \pm 0.221 \pm 0.007 \pm 0.330$
	$1e, 1\mu$	$0.676 \pm 0.154 \pm 0.004 \pm 0.330$
	$2e$	$0.676 \pm 0.154 \pm 0.096 \pm 0.330$
	2μ	$0.676 \pm 0.154 \pm 0.103 \pm 0.330$
$\leq$1 b-tag	0ℓ	$0.822 \pm 0.144 \pm 0.022 \pm 0.180$
	$1e, 1\mu$	$0.882 \pm 0.044 \pm 0.003 \pm 0.120$
	$2e$	$0.882 \pm 0.044 \pm 0.099 \pm 0.120$
	2μ	$0.882 \pm 0.044 \pm 0.107 \pm 0.120$

Table 11: Scale factors (SF) derived for the normalization of the $t\bar{t}$ and S_{T} backgrounds for different event categories. Uncertainties due to the limited size of the event samples (stat) and systematic effects (syst) are reported as well.

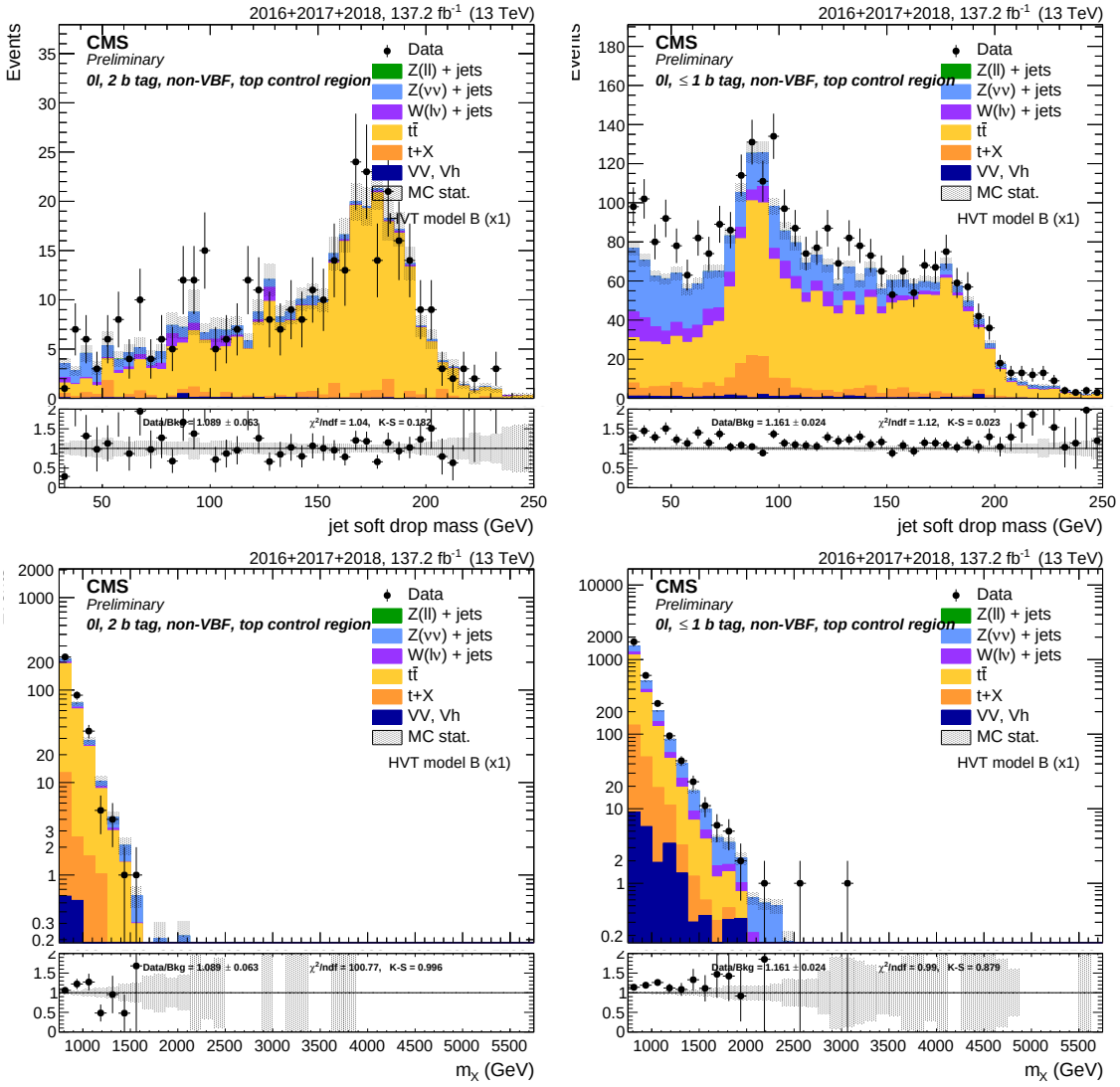

Figure 25: Jet mass (upper) and m_X distributions (lower) in the 0-lepton, 2 b-tagging (left) and $\leq$1 b-tagging (right) top-quark control regions.

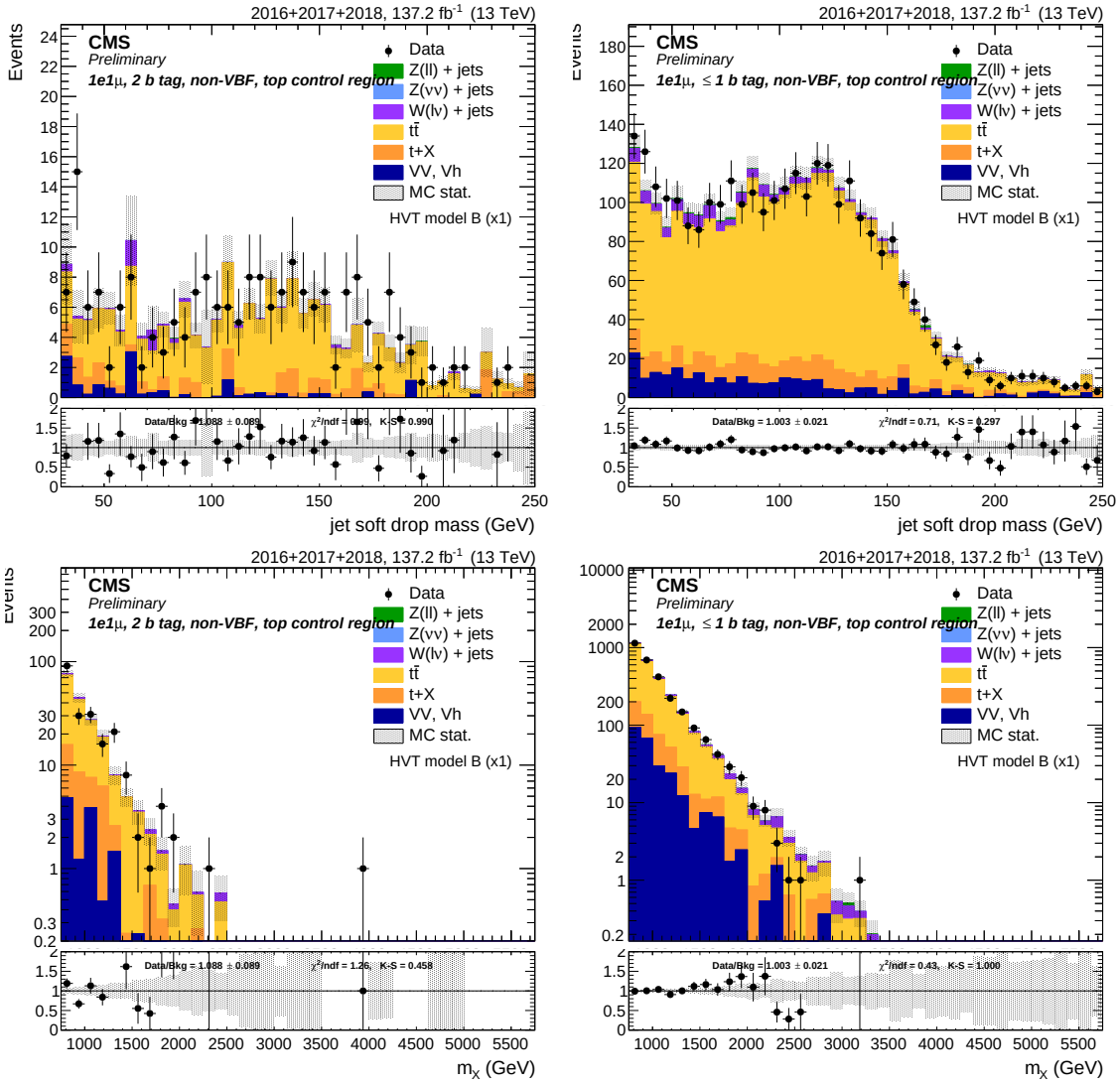

Figure 26: Jet mass (upper) and m_X distributions (lower) in the 2-lepton 2 b-tagging (left) and $\leq$1 b-tagging (right) top-quark control regions.

9 Background estimation

The *alpha* method is used to be less dependent on the Monte Carlo simulation for the m_X background estimation, due to many systematic uncertainties, which are hard to control in the boosted regime. For the α method, the jet mass distribution is split into a signal-enriched region, called *signal region* (SR) and a signal-depleted region, named *sidebands region* (SB). First the V+jets background normalization is extracted from data in the sideband region. Then, the V+jets background shape is determined in the sideband region from data by subtracting the $t\bar{t}$ and VV contributions and then extrapolating to the signal region using the α function, which is defined as the ratio of the simulated m_X shape in the SR and SB:

$$\alpha(m_X) = \frac{N_{SR}^{Vjet}(m_X)}{N_{SB}^{Vjet}(m_X)}$$

The soft-drop, PUPPI-corrected jet mass m_j (see section 5.7.1) is used to specify the regions with the cuts defined in section 7. The Z mass window is not used for the background estimation or the signal to avoid unblinding a potential lower mass $X \to VV$ signal.

The main background is V+jets, whose modelling with Monte Carlo is not considered trustworthy. The subdominant backgrounds are $t\bar{t}$ with single-top-quark and VV, which are considered well-modeled in Monte Carlo. In the zero-lepton channels, the contribution from $t\bar{t}$ can be of the same order of magnitude as the main background, therefore the normalization needs to be validated on data using top-quark scale factors as described in section 8. The scale factors are applied to the normalization of $t\bar{t}$ for the alpha method. The shape and normalization of the VV background are taken from simulation. The background predictions are derived for each category separately, dividing the electron/muon channel and the b-tagging categories, in order to reduce systematic uncertainties due to leptonic triggers, identification, isolation and b-tagging efficiencies.

9.1 Background normalization

The background normalization has to be estimated for the background prediction. The jet-mass distribution has a different shape for the three main backgrounds (V+jets, $t\bar{t}$ and single-top-quarks, VV including VH). Therefore each background is fitted with a different functional form. The number of expected events in the signal region is estimated using equation 4,

$$N_{SR}^{data} = \left[N_{SB}^{data} - N_{SB}^{Top} - N_{SB}^{VV}\right] \times \left[\frac{N_{SR}^{Vjet}}{N_{SB}^{Vjet}}\right] + N_{SR}^{Top} + N_{SR}^{VV}\,, \tag{4}$$

with N being the number of events.

The functional forms are constructed reflecting the physics properties of each background. The V +jet background has a smoothly falling background without any

peaks. The jet mass distribution of the VV background has peaks corresponding to the hadronic decays of W and Z bosons and possibly a third one for the Higgs boson. In some categories they might not all be seen due to a lack of statistics or small cross section. The $t\bar{t}$ background and single-top-quark backgrounds have two peaks corresponding to the $W \to q\bar{q}$ decays and the all-hadronic top quark decays $t \to Wb \to q\bar{q}b$. The peak from $W \to q\bar{q}$ decays cannot be seen in the 2 b-tagging category as the AK8 jets cluster both b-quarks from the top quark decay. The functional forms are listed below and in Table 12 for each category.

Pol: a polynomial with a variable number of parameters:

$$F_{\text{Pol}}(x) = a_0 \cdot x + a_2 \cdot x^2 + a_3 \cdot x^3$$

Gaus: one gaussian:

$$F_{\text{Gaus}}(x) = \cdot e^{2(x-a)^2/b}$$

Gaus2: two gaussians:

$$F_{\text{Gaus2}}(x) = f_0 \cdot e^{2(x-a)^2/b} + (1 - f_0) \cdot e^{2(x-c)^2/d}$$

Gaus3: three gaussians:

$$F_{\text{Gaus3}}(x) = f_0 \cdot e^{2(x-a)^2/b} + f_1 \cdot e^{2(x-c)^2/d} + (1 - f_0 - f_1) \cdot e^{2(x-e)^2/g}$$

ExpGaus: an exponential plus one gaussian:

$$F_{\text{ExpGaus}}(x) = f_0 \cdot e^{ax} + (1 - f_0) \cdot e^{2(x-b)^2/c}$$

ExpGaus2: an exponential plus two gaussians:

$$F_{\text{ExpGaus2}}(x) = f_0 \cdot e^{ax} + f_1 \cdot e^{2(x-b)^2/c} + (1 - f_0 - f_1) \cdot e^{2(x-d)^2/e}$$

ErfExpGaus: an error function plus one gaussian:

$$F_{\text{ExpGaus}}(x) = f_0 \cdot F_{\text{ErfExp}}(x, a, b, c) + (1 - f_0) \cdot e^{2(x-d)^2/e}$$

ErfExpGaus2: an error function plus two gaussians:

$$F_{\text{ExpGaus2}}(x) = f_0 \cdot F_{\text{ErfExp}}(x, a, b, c) + f_1 \cdot e^{2(x-d)^2/e} + (1 - f_0 - f_1) \cdot e^{2(x-f)^2/g}$$

The number of parameters of the polynomial used to fit the data is derived with a Fisher test and reported in Table 13. The categories fitted with many parameters contain more statistics than the other categories.

Figure 27 shows the fits to the jet mass distribution for the V+jets, VV and $t\bar{t}$ backgrounds for the 0ℓ, 2 b-tagging, non-VBF category, the same is done for all other categories. Figures 28 and 29 show the jet mass distributions with the backgrounds combined for all categories. In Table 14 the observed and expected background yield in the signal region is reported for each category. The observed number of events agree in general with the expected background number of events, only the 0ℓ, 2 b-tagging, non-VBF category shows a small excess.

category		V+jets	alt. V+jets	$t\bar{t}$	VV
2 b-tag	0ℓ	Pol5	ExpGaus	Gaus2	ErfExpGaus2
	$2e$	Pol5	ExpGaus	Gaus2	ErfExpGaus2
	2μ	Pol5	ExpGaus	Gaus2	ExpGaus2
$\leq$1 b-tag	0ℓ	Pol5	ExpGaus	Gaus3	ErfExpGaus
	$2e$	Pol5	ExpGaus	Gaus	ExpGaus
	2μ	Pol5	ExpGaus	Gaus	ErfExpGaus
2 b-tag VBF	0ℓ	Pol5	ExpGaus	Gaus2	ErfExpGaus
	$2e$	Pol5	ExpGaus	Gaus	ExpGaus
	2μ	Pol5	ExpGaus	Gaus2	ExpGaus
$\leq$1 b-tag VBF	0ℓ	Pol5	ExpGaus	Gaus3	ErfExpGaus
	$2e$	Pol5	ExpGaus	ErfExpGaus	ExpGaus
	2μ	Pol5	ExpGaus	Gaus	ExpGaus

Table 12: Chosen functions to fit the jet mass distribution for each category.

category		N. of par.
2 b-tag	0ℓ	5
	$2e$	2
	2μ	2
$\leq$1 b-tag	0ℓ	4
	$2e$	3
	2μ	2
2 b-tag VBF	0ℓ	2
	$2e$	2
	2μ	2
$\leq$1 b-tag VBF	0ℓ	2
	$2e$	2
	2μ	2

Table 13: Number of parameters of the polynomial used to fit the data, derived with a Fisher test.

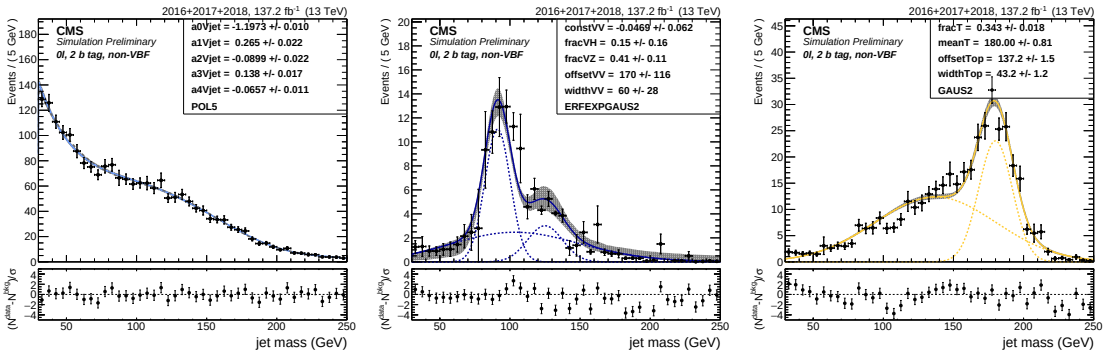

Figure 27: Fit to the simulated m_j in the 0 lepton, 2 b-tagging category for the three backgrounds: V+jets (left), VV (center), Top-quark (right).

category		V+jets (±fit) (±alt)	$t\bar{t}$, S_{T}	VV	Bkg. sum	Observed
2 b-tag	0ℓ	$374 \pm 34 \pm 20$	68 ± 8	31 ± 10	474 ± 42	549
	$2e$	$54 \pm 5 \pm 8$	3.1 ± 0.4	7.9 ± 1.9	65 ± 10	57
	2μ	$60 \pm 5 \pm 1$	3.2 ± 0.6	9.1 ± 2.1	72 ± 5	91
$\leq$1 b-tag	0ℓ	$637 \pm 35 \pm 51$	7.3 ± 0.9	15 ± 4	659 ± 61	697
	$2e$	$113 \pm 14 \pm 27$	1.6 ± 0.2	7.2 ± 1.7	122 ± 31	130
	2μ	$167 \pm 8 \pm 10$	1.8 ± 0.2	8.0 ± 1.8	177 ± 13	154
2 b-tag VBF	0ℓ	$28 \pm 3 \pm 3$	4.3 ± 2.0	0.9 ± 0.6	33 ± 5	26
	$2e$	$7.3 \pm 2.0 \pm 2.0$	0.4 ± 0.2	0.4 ± 0.1	8.1 ± 2.8	10
	2μ	$6.0 \pm 1.7 \pm 0.2$	0.4 ± 0.2	0.5 ± 0.1	7.0 ± 1.7	8.0
$\leq$1 b-tag VBF	0ℓ	$486 \pm 13 \pm 72$	25 ± 6	6.3 ± 1.5	517 ± 73	572
	$2e$	$137 \pm 7 \pm 7$	4.8 ± 1.5	6.4 ± 1.5	148 ± 10	168
	2μ	$171 \pm 8 \pm 6$	4.5 ± 1.1	7.7 ± 1.8	183 ± 10	222

Table 14: Expected and observed numbers of events in the signal region. The V+jets uncertainties include the variation of the parameters within the fit uncertainties and the correlation between them (fit), and the uncertainty due to the variation of the fit function (alt). The $t\bar{t}$ and S_{T} uncertainty includes the fit uncertainty (as described for V+jets) and the statistical and systematic uncertainty of the top-quark scale factor. The VV uncertainty includes the uncertainty due to the fit and the systematic uncertainty affecting the normalization.

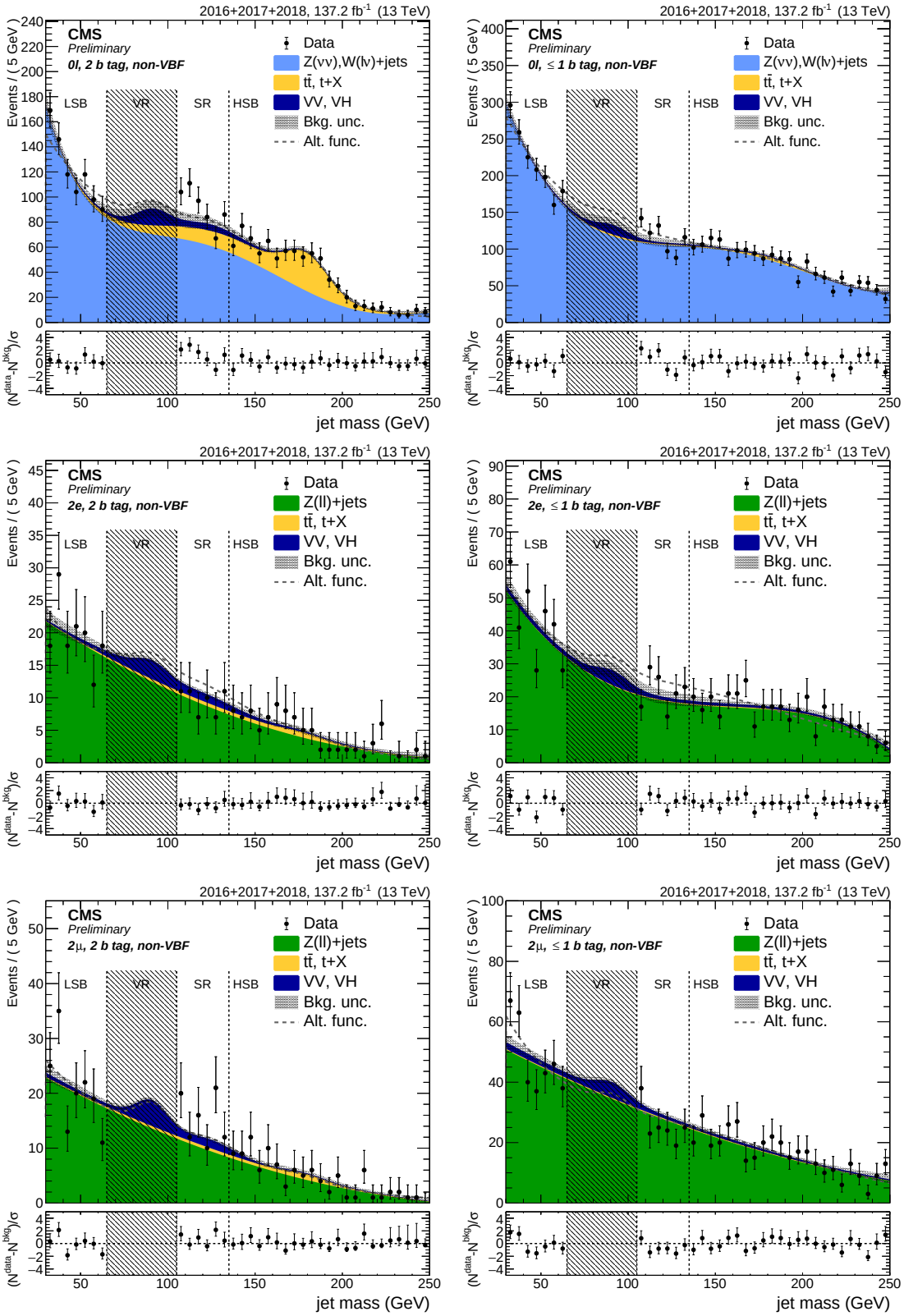

Figure 28: Fit to data m_{j} in the 2 b-tagging (left) and $\leq$1 b-tagging (right), 0 lepton (top), 2 electron (middle) and 2 muon (bottom) category. The observed data are indicated by black markers. The bottom panel shows for each bin $(N^{data} - N^{bkg})/\sigma$, where σ is the statistical uncertainty in data.

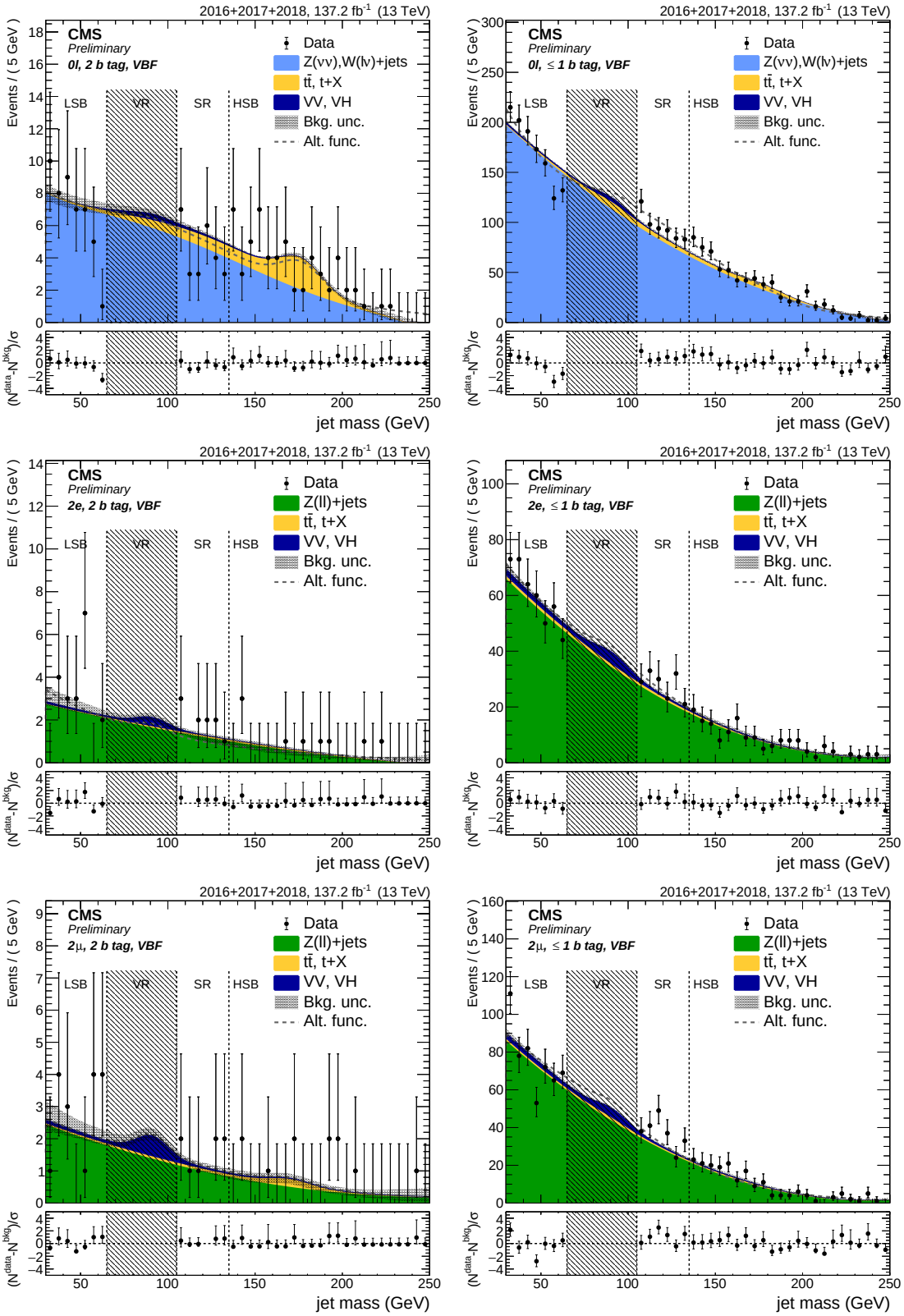

Figure 29: Fit to data m_{j} in the VBF, 2 b-tagging (left) and $\leq$1 b-tagging (right), 0 lepton (top), 2 electron (middle) and 2 muon (bottom) category. The observed data are indicated by black markers. The bottom panel shows for each bin $(N^{data}-N^{bkg})/\sigma$, where σ is the statistical uncertainty in data.

9.2 Background shape

The mass of the heavy resonance (m_X) is parametrized separately for V+jets, $t\bar{t}$ and VV by fitting functions to the simulated m_X (or m_{T}^X for zero lepton) distribution in the sideband and signal region. The normalization for V+jets is determined from the m_{j} fit, $t\bar{t}$ is normalized by the top-quark control region and VV is normalized to the integrated luminosity. The alpha function is derived using the V+jets function in the signal and in the sideband region:

$$\alpha(m_X) = \frac{N_{SR}^{Vjet}(m_X)}{N_{SB}^{Vjet}(m_X)}$$

The V+jets background is determined by a fit to data in the sideband region, after subtracting the $t\bar{t}$ and VV contributions from data. This shape is multiplied by the α-function to derive the V+jets background in the signal region. Adding the $t\bar{t}$ and VV contributions determines the total background estimation in the signal region, as shown in formula 5.

$$N_{SR}^{data}(m_X) = \left[N_{SB}^{data}(m_X) - N_{SB}^{Top}(m_X) - N_{SB}^{VV}(m_X)\right] \times \alpha(m_X) + N_{SR}^{Top}(m_X) + N_{SR}^{VV}(m_X), \tag{5}$$

where N denotes the function.

The m_X distributions are parametrized by using the following functions:

ExpN: a product of two exponentials:

$$F_{\mathrm{ExpN}}(x) = e^{ax+b/x}$$

ExpTail: a modified exponential function with an additional parameter to model the exponential tails:

$$F_{\mathrm{ExpTail}}(x) = e^{-x/(a+bx)}$$

The V+jets, $t\bar{t}$ and VV backgrounds are parametrized by the **ExpN** function. The V+jets background has **ExpTail** as an alternative function, which is used to determine the uncertainty due to the choice of the function by deriving an alternative α-function. Figures 30, 31 and 32 show the process for the 0ℓ, 2 b-tagging, non-VBF category. The same is done for all other categories.

9.3 Background prediction

The background predictions in the signal range derived with the α-method are compared to data and shown for each category in Figures 33 and 34.

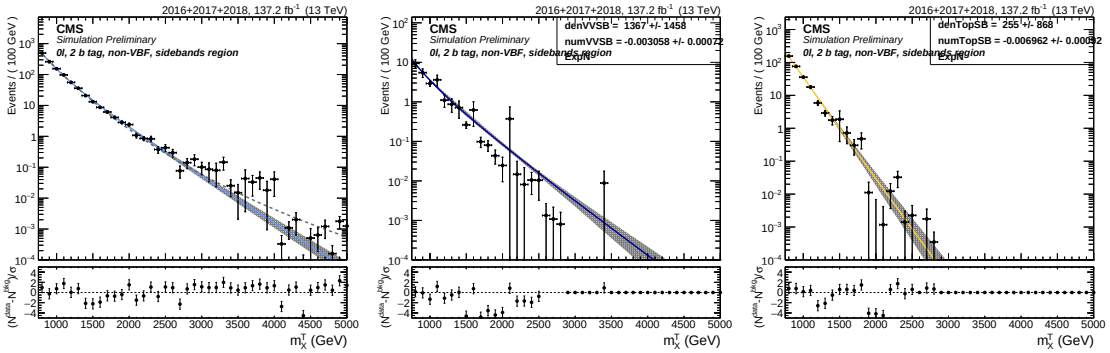

Figure 30: 0 leptons, 2 b-tagging category. Fits to the simulated background components V+jets (left), VV (center), $t\bar{t}$ (right) in the sidebands (SB).

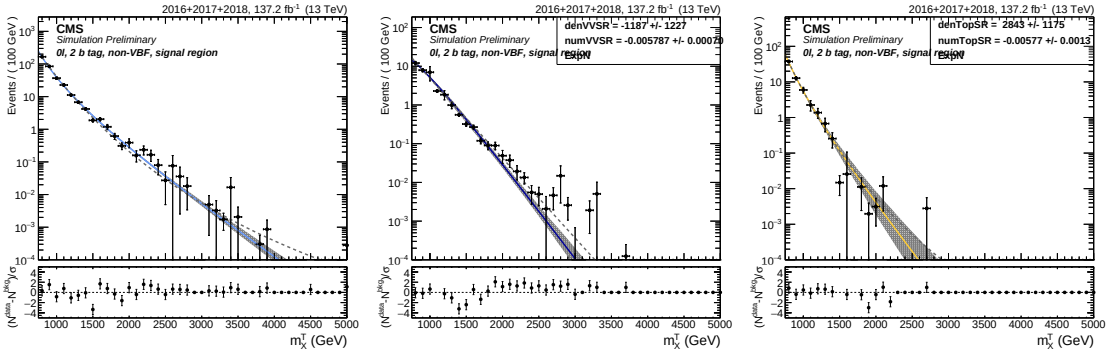

Figure 31: 0 leptons, 2 b-tagging category. Fits to the simulated background components V+jets (left), VV (center), $t\bar{t}$ (right) in the signal region (SR).

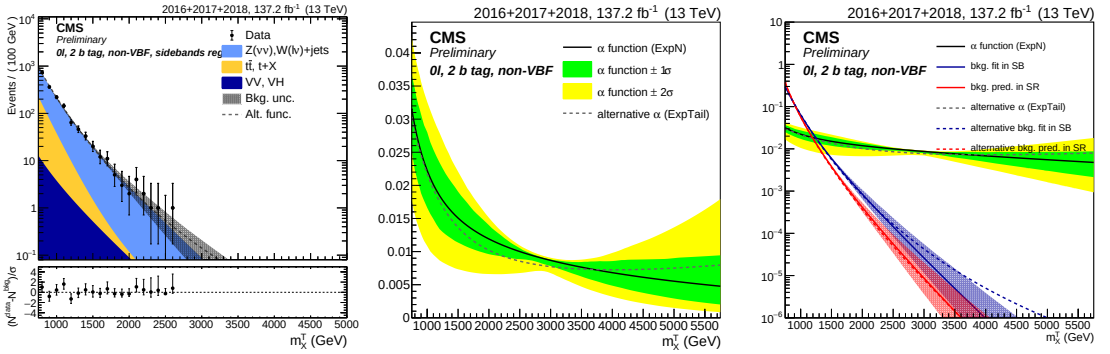

Figure 32: 0 leptons, 2 b-tagging category. Fit to data in the SB (left), alpha function (center), and alpha function compared to the background shape in both SB and SR (right). The black line, with the corresponding 1σ (green) and 2σ (yellow) uncertainty bands, represents the α-function. The gray line is the alternative α-function. The blue and red lines represent the estimated background in the SB and SR, respectively, with both the main (solid line) and alternative (dotted line) parametrization.

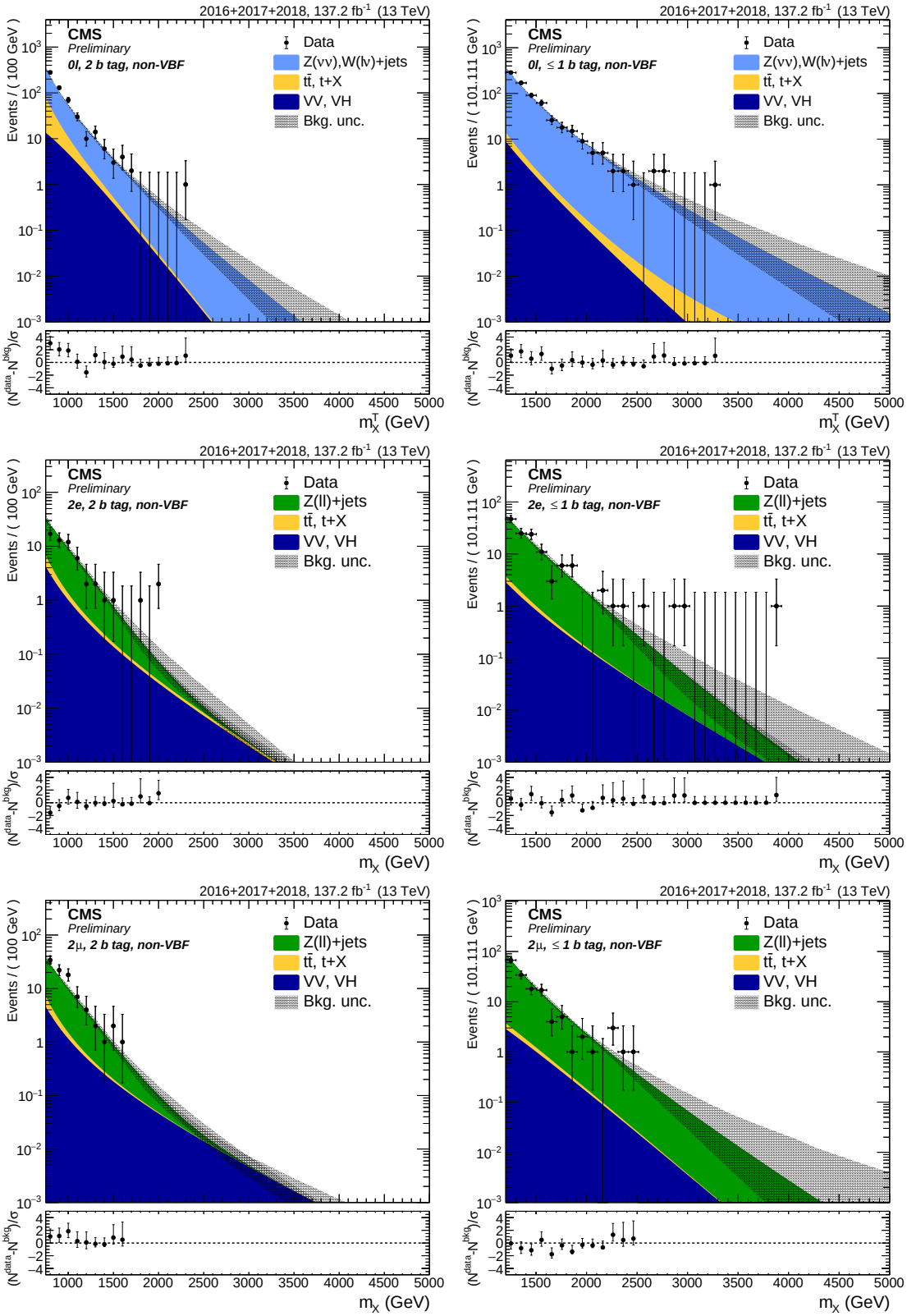

Figure 33: Expected background with the α method in the 0 lepton (top), 2 electrons (center) and 2 muons (bottom) in the 2 b-tagging (left) and $\leq$1 b-tagging (right) non-VBF category. The observed data are indicated by black markers. The bottom panel shows for each bin $(N^{data} - N^{bkg})/\sigma$, where σ is the statistical uncertainty in data.

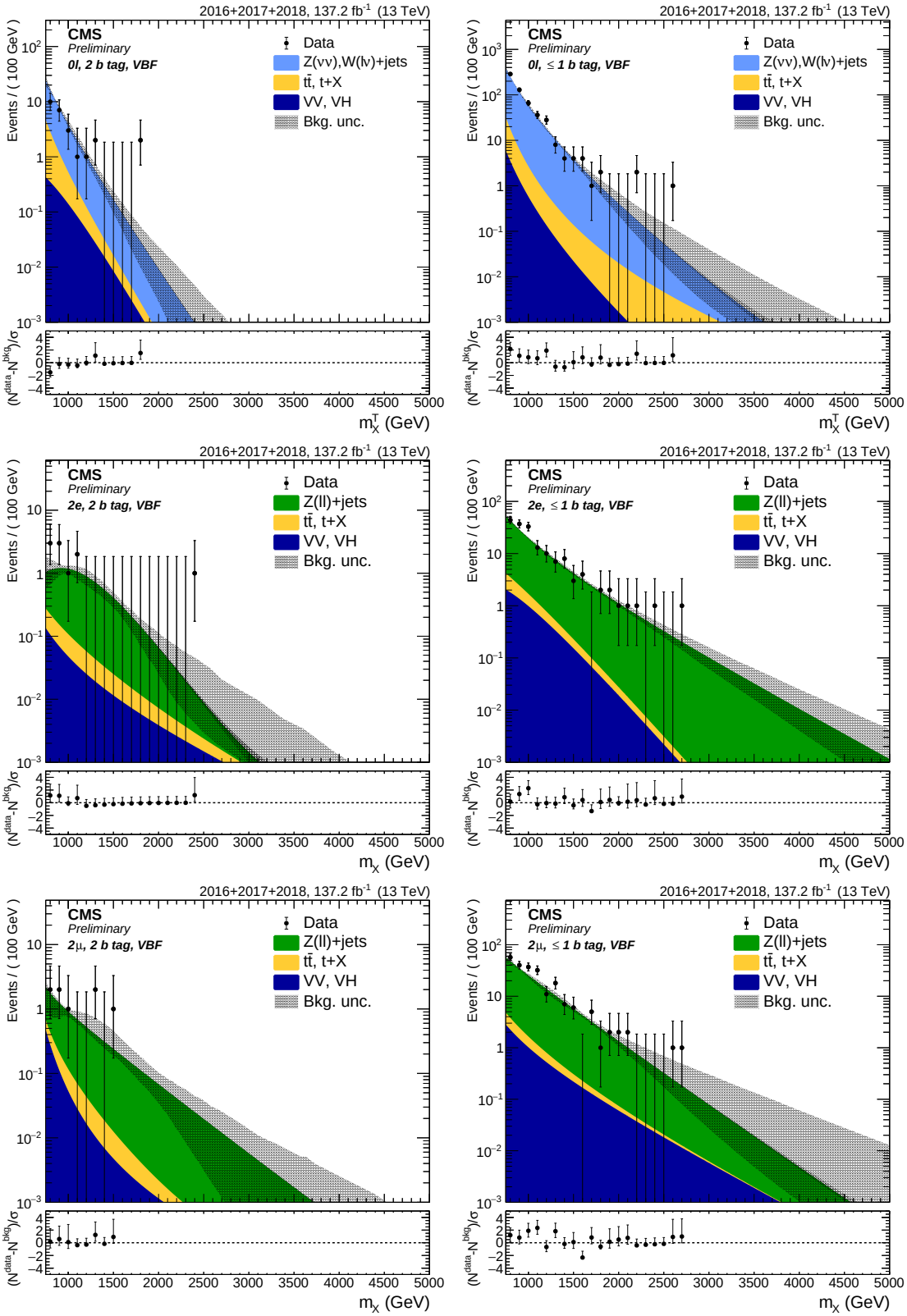

Figure 34: Expected background with the α method in the 0 lepton (top), 2 electrons (center) and 2 muons (bottom) in the 2 b-tagging (left) and $\leq$1 b-tagging (right) VBF category. The observed data are indicated by black markers. The bottom panel shows for each bin $(N^{data} - N^{bkg})/\sigma$, where σ is the statistical uncertainty in data.

9.4 Alpha method validation

The α-method is validated by comparing the background prediction in a pseudo signal region to data. The lower sideband is split into two regions: $30-50$ GeV (LSB) acts as the lower sideband region and $50-65$ GeV as the pseudo signal region. The upper sideband is not modified with respect to the standard α-method. In Figures 35 and Table 15 the predicted shape and normalization extracted from the α-method are compared to data. Both the normalization and the shape show an acceptable agreement to data, confirming the reliability of the α-method to extract the V+jets background.

category		V +jets (±stat) (±syst)	$t\bar{t}$,t+X	VV	Bkg. sum	Observed
2 b-tag	0ℓ	$304 \pm 13 \pm 5$	7.0 ± 1.0	4.5 ± 1.4	315 ± 14	306 ± 17
	$2e$	$50 \pm 5 \pm 3$	0.6 ± 0.1	2.1 ± 0.5	52 ± 6	49 ± 7
	2μ	$54 \pm 5 \pm 1$	0.8 ± 0.2	1.8 ± 0.4	57 ± 5	52 ± 7
$\leq$1 b-tag	0ℓ	$561 \pm 19 \pm 16$	2.0 ± 0.3	6.9 ± 1.9	569 ± 25	536 ± 23
	$2e$	$98 \pm 7 \pm 10$	0.3 ± 0.1	4.4 ± 1.0	103 ± 12	115 ± 11
	2μ	$111 \pm 7 \pm 10$	0.9 ± 0.4	5.5 ± 1.3	117 ± 13	126 ± 11
2 b-tag VBF	0ℓ	$24.5 \pm 3.2 \pm 0.5$	0.5 ± 0.2	0.2 ± 0.1	25 ± 3	13 ± 4
	$2e$	$5.6 \pm 1.6 \pm 0.1$	0.1 ± 0.1	0.3 ± 0.1	6.0 ± 1.6	9.0 ± 3.0
	2μ	$4.4 \pm 1.6 \pm 0.2$	0.2 ± 0.1	0.3 ± 0.1	4.9 ± 1.6	9.0 ± 3.0
$\leq$1 b-tag VBF	0ℓ	$466 \pm 15 \pm 3$	5.9 ± 1.6	5.0 ± 1.4	477 ± 15	412 ± 20
	$2e$	$157 \pm 9 \pm 1$	3.4 ± 1.0	5.7 ± 1.3	166 ± 10	149 ± 12
	2μ	$210 \pm 11 \pm 4$	2.9 ± 0.8	7.5 ± 1.7	220 ± 12	206 ± 14

Table 15: Expected and observed background yield in the pseudo signal jet mass region ($50 < m_j < 65$ GeV)

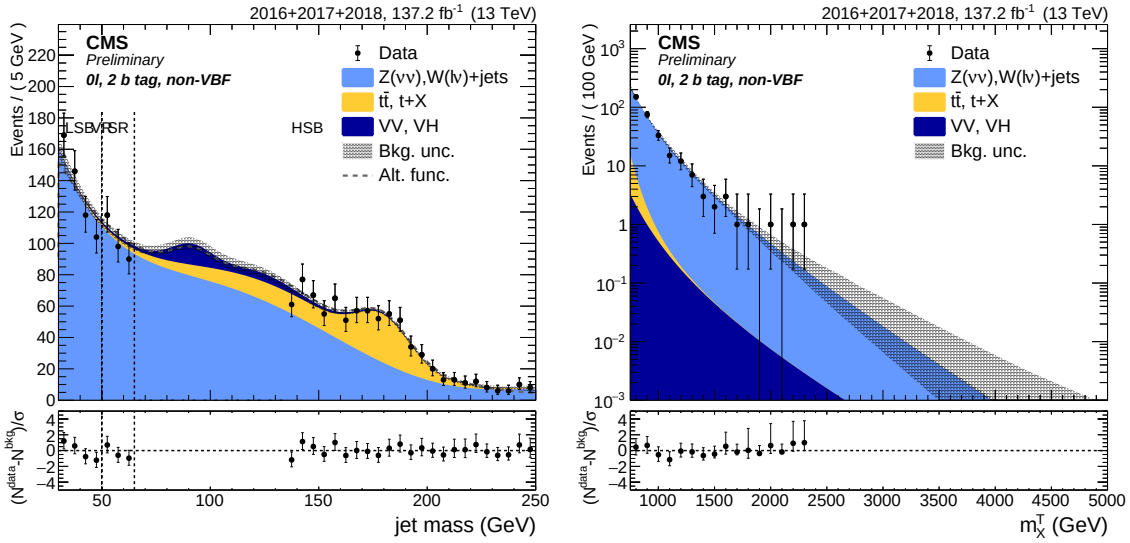

Figure 35: Fit to the m_j (left) and to the m_X (right) distribution in data in the sidebands for the 0ℓ, b-tagging, non-VBF category. The SR is replaced by splitting the lower m_j sideband ($50 < m_j < 65$ GeV) for validation purposes.

10 Signal modelling

The simulated signal mass points are fitted in the signal range with a *Crystal Ball* function, which is a gaussian peak with a lower tail. The parametrization of intermediate mass points is determined by linear interpolation of shape parameters from fitting the generated mass points. A spline is used to determine the normalization of the intermediate mass points by interpolating the signal normalization. The Spline method is cross checked using a polynomial. The signal modelling is shown for five masspoints of the 0ℓ,2 b-tagging, non-VBF category in Figure 36.

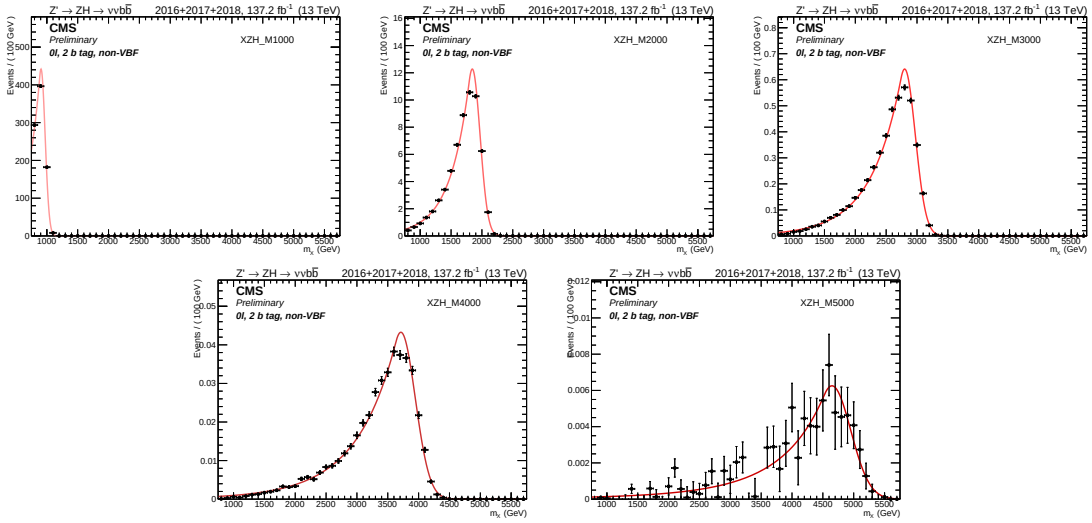

Figure 36: Signal fits for a Z' with mass 1 to 5 TeV in the 0ℓ, 2 b-tagging, non-VBF category.

In Figure 37 the signal templates for all non VBF categories are shown as a function of the generated mass m_X. The transverse mass (see section 6.1) used for the 0ℓ categories results in a larger width of the signal peaks.

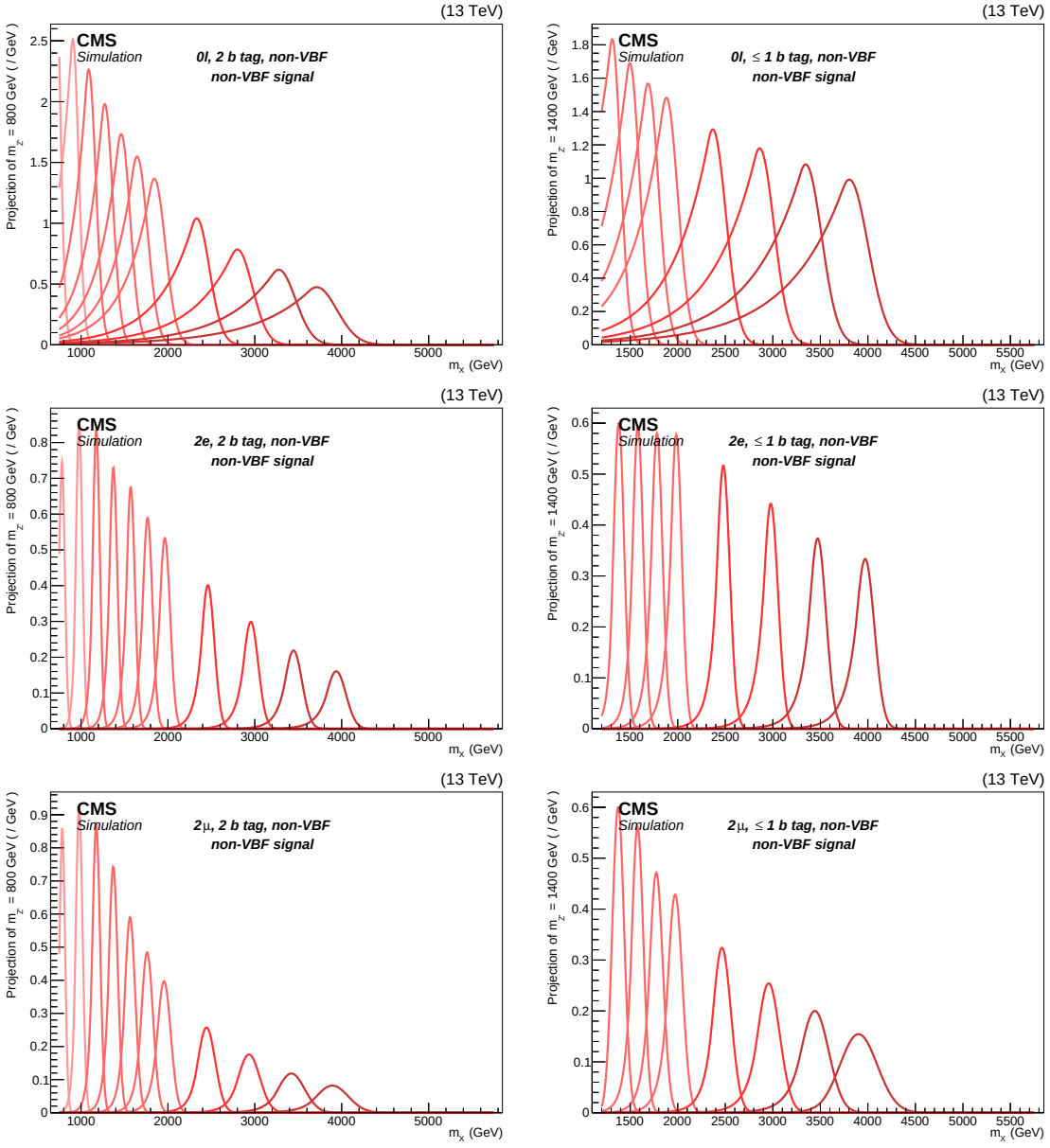

Figure 37: Signal templates as a function of the generated mass m_X, separately for 0 lepton (top), 2 electron (center) and 2 muon (bottom) in the 2 b-tagging (left) and $\leq$1 b-tagging (right) category.

11 Systematic uncertainties

This section reports all systematic uncertainties affecting the background and signal prediction. Most of the systematic uncertainties are dedicated to samples not normalized to data or with a shape taken from simulation. The uncertainties are correlated between years as they are derived using the combined simulated events from 2016, 2017 and 2018. Luminosity is treated as uncorrelated between years.

11.1 Normalization uncertainties

The normalization and shape of the V+jets background are taken from data. The $t\bar{t}$ background is normalized with data, but the shape is taken from simulation. The VV background is derived only with simulation, therefore the normalization has its own systematic uncertainty. The systematic uncertainties of the normalization for V+jets and $t\bar{t}$ are derived by varying the parameters within the fit uncertainties and taking into account the correlation between them as described in section 9.1. The choice of the function introduces an additional systematic uncertainty to the normalization of V+jets, which is estimated by using an alternative function for V+jets to derive the normalization (Sec. 9.1). The difference in the predicted normalization is taken as the systematic uncertainty and reported in Table 14 for each category.

The normalization uncertainty for $t\bar{t}$ and single-top-quark is caused by the limited statistics in the top-quark control region and the extrapolation from the top-quark control region to the signal region. The systematic uncertainty for the 0ℓ channel is derived varying the b-tagging scale factor. For the 2ℓ categories, the uncertainties on the electron and muon identification and for the 2 μ channel additionally the electron and muon trigger uncertainties are taken into account. The values are reported in Table 11.

The single-top-quark normalization uncertainties have to be taken into account as they affect the top-quark scale factor. The impact of the PDF scale, PDF acceptance and QCD scale on the single-top-quark normalization and, considering the single-top-quark contribution in the top-quark control region, on the top-quark scale factors is reported in Table 16.

The diboson normalization uncertainty depends on the cross section uncertainty and is calculated to be 2.2% (PDF + α_s) and 2.5% (QCD scales). Additional uncertainties due to the extrapolation to the analysis phase-space are applied and reported in Table 16.

11.2 Shape uncertainties

The shape uncertainties of the V+jets background are affected by the parameter error of the simultaneous fit to m_X in data in the sideband region and by the α-function, which depends on the fits to m_X in the V+jets background in the signal and sideband regions. These uncertainties are propagated to the shape of the V+jets background

Source	Single-top-quark	Top-quark SF	VV
PDF scale	0.4%	0.024%	1.7%
PDF acceptance	2.2%	0.132%	2.0%
QCD scales	16.6%	0.996%	16.4%

Table 16: Summary of secondary background normalization uncertainties. Single-top-quark uncertainties affect the top-quark scale factors, diboson uncertainties impact the normalization in the signal regions.

in the signal region. Before the likelihood fit, the parameters are decorrelated through a linear transformation.

The choice of the function introduces a bias, which can be validated using an alternative and orthogonal set of functions for the background prediction. The alternative alpha function and the alternative background prediction are within the uncertainties of the nominal alpha and background prediction, showing that the bias is small.

11.3 Triggers

The trigger uncertainties are evaluated by shifting the trigger scale factor by one standard deviation as reported in Section 5.2. The trigger uncertainties are reported in Table 17. A flat 4% systematic uncertainty is added for the muon trigger to account for the uncertainty on the scale factors and for the impact of pre-triggering [62].

11.4 Leptons

The systematic uncertainties originating from the identification and isolation of leptons are evaluated by varying the respective scale factors (Section 5). For muons an additional flat uncertainty of 1% for identification and 2% for isolation is added [62]. The uncertainties are reported in Table 17. The uncertainties do not depend on the heavy resonance mass and are considered flat. Uncertainties for different lepton flavour are considered uncorrelated, for the same lepton flavour they are considered correlated. In the 0ℓ channel the systematic uncertainties of 1% for the muons, 1% for the electrons and 3% for the taus are added to account for the different veto efficiencies.

	Trigger	Id+Iso (2ℓ)
Electrons	0.9%	3.6%
Muons	3% (4%)	1.9% (3%)

Table 17: Summary of lepton normalization uncertainties. Number in parenthesis are systematic uncertainties.

Uncertainties on lepton momentum scale and resolution have an affect on the signal shape by changing the mean or resolution of the Crystal Ball function. For the

muons, η and ϕ dependent scale factors are evaluated in the framework of $Z' \to \mu\mu$ searches and used to correct the curvature of each muon by applying the scale factors to the muon p_T. After the correction is applied to both muons, the heavy resonance mass is recalculated. The uncertainties correspond to the relative difference of the mean, the width and the integral between the m_X distribution with and without the correction. For the electrons, the electron scale and resolution corrections are propagated to the m_X distribution. The uncertainties are extracted from the m_X distribution in the same way as for the muons. The lepton scale uncertainties are reported in Table 18. The resolution uncertainties are omitted as they only have negligible impact on the normalization.

Scale unc.	e		μ	
m_X	1 TeV	4 TeV	1 TeV	4 TeV
Δ events	1.%	1.%	2.%	0.5%
Δ mean	<0.1%	<0.1%	<0.1%	<0.1%
Δ RMS	0.1%	0.1%	5%	3%

Table 18: Summary of lepton scale uncertainties. The resolution uncertainties are omitted as they have negligible impact on the normalization.

11.5 Jet energy scale and resolution

The jet uncertainties are evaluated by varying the jet energy corrections (jet energy scale (JES) and resolution (JER)) up and down by one standard deviation. The correction for the jet energy scale is derived by shifting the p_T of the jets. The resolution is smeared with a hybrid method: If a matching particle-level jet is found, the scaling method is used, otherwise the stochastic method. The jet energy corrections are considered correlated between the years. The impact of the jet energy corrections to the normalization in the signal region is evaluated by comparing the m_X distribution after applying the jet energy corrections. The effect of the jet energy scale on the normalization results in a systematic uncertainty of $\pm 1.2\%$ for the diboson background and is small ($\lesssim 1\%$) for the signal samples. The effect of the jet energy resolution on the normalization is small $\sim 1\%$ for the diboson and signal samples.

The jet energy correction uncertainties also impact the signal shape. The uncertainties are evaluated to be 0.1% for the mean and 1% for the width of the Crystal Ball function.

11.6 Jet mass scale and resolution

The jet mass uncertainties are evaluated by varying the jet mass scale and resolution and comparing the PUPPI soft-drop jet mass distributions in the signal region, and shown in Fig. 38. The jet mass uncertainty for the signal samples is 0.6% for the scale and 9% for the resolution. The same uncertainties are also applied to the diboson background.

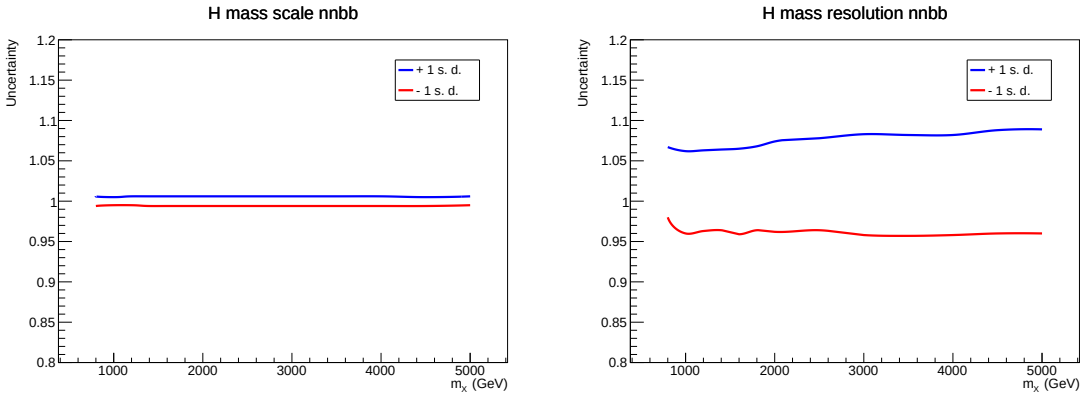

Figure 38: Signal normalization variations obtained varying the jet mass scale (left) and resolution (right).

11.7 Higgs boson mass extrapolation uncertainty

The Higgs boson is tagged based on a jet mass range, which depends on the choice of parton showering algorithm, introducing a systematic uncertainty. The uncertainty is derived by calculating the ratio of efficiency for tagging a W and a Higgs boson based on a mass range around the nominal value, for a Bulk Graviton decaying to WW and HH. This is done for the PYTHIA and HERWIG showering algorithms. The double ratio R_{HERWIG}/R_{PYTHIA} shows the impact of the showering algorithm on the ratio of efficiency for tagging a W and a Higgs boson based on a mass range. This study is done for hadronically decaying W and Higgs bosons, but the results also apply to the leptonic final states. The results are shown in Figure 39 for different substructure selections. The deviation from the double ratio to 1 is taken as the systematic uncertainty and is estimated to be 6%.

11.8 B-tagging

The b-tagging uncertainty is evaluated by varying the b-tagging scale factor applied to each jet depending on p_T and η [63]. The uncertainty on the signal normalization is shown in Figure 40 for the 2 b-tagging and the $\leq$1 b-tagging categories. For the 2 b-tagging category the uncertainty ranges between 5% and 15%, and between 0.7% and 6% for the $\leq$1 b-tagging category. The b-tagging uncertainties are considered correlated between backgrounds, but anti-correlated between b-tagging categories.

The b-tagging uncertainty also has an effect on the $t\bar{t}$ normalization in the 0ℓ channel, due to the inversion of the b-tagging veto for the derivation of the top-quark scale factors. The top-quark scale factors are re-evaluated after varying the b-tagging scale factor and the difference in the top-quark scale factors is taken as the systematic uncertainty. The uncertainty is evaluated to be 1.4% and correlated with the b-tagging uncertainty for the signal.

The diboson background normalization has a 0.6% uncertainty applied due to the b-tagging veto as well as a 6.5% uncertainty in the 2 b-tagging category and a 0.6% uncertainty in the $\leq$1 b-tagging category due to b-tagging the Higgs-boson jet. The

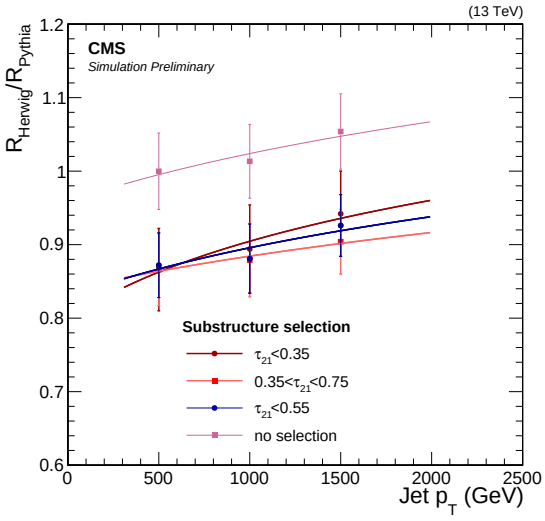

Figure 39: R_{HERWIG}/R_{PYTHIA} as function of the jet p_T for different substructure selections, and parametrized as a function of the jet p_T. The function chosen to fit the points is $a \cdot log(p_T + b)$. Without a τ_{21} selection, the uncertainty is assumed to the maximum between the central value and the end of the uncertainty band, which results in a flat 6% uncertainty over the full p_T range.

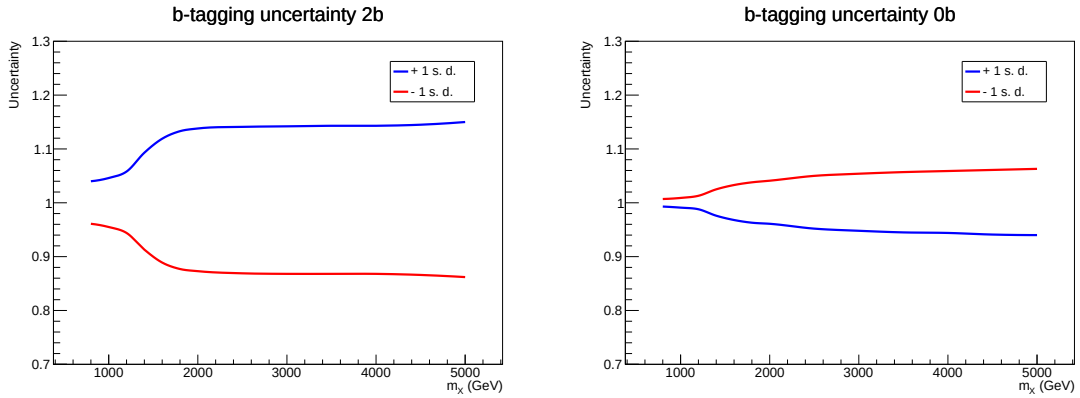

Figure 40: Signal normalization uncertainties obtained varying the b-tagging scale factors by one standard deviation in the 2 (left) and ≤1 (right) b-tagging categories. The colors indicate the upward and downward variations, which are anti-correlated between the categories.

uncertainties due to the Higgs-boson tagging and the b-tagging veto are considered anti-correlated for the 2 b-tagging and correlated for the ≤1 b-tagging category.

11.9 Missing Energy

The E_T^{miss} is built from all the reconstructed particles in the detector and therefore affected by the energy scale and resolution of them. The uncertainties were derived in the analysis B2G-17-004 [1] by propagating the scales and resolutions of the reconstructed objects to the E_T^{miss}. The evaluated uncertainty was 1%, therefore the

E_T^{miss} uncertainty is not considered for this analysis.

11.10 Prefire

The ECAL crystals are darkening with time, leading to a gradual timing shift. In 2016 and 2017 this timing shift was not properly taken into account for the level-one triggers, erroneously associating some triggers to the previous bunch crossing. Prefire weights were derived, showing only a minimal effect on the signal normalization. The V+jets background is not affected as it is normalized with data. The effect on the signal normalization results in a systematic uncertainty of 1%. The Prefire weights for the 1 TeV signal are shown in Figure 41 for the non VBF and the VBF category.

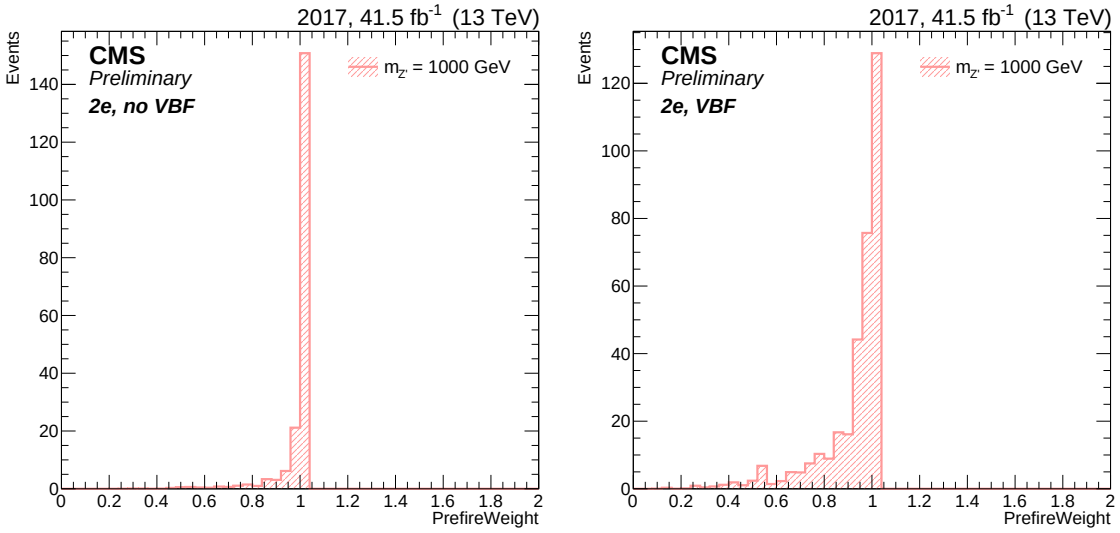

Figure 41: Prefire weight for inclusive $Z \to ee$ category (left) and inclusive VBF $Z \to ee$ category (right).

11.11 Pile-up

The minimum bias cross section at 13 TeV is only known with a limited precision and is used to derive the primary vertices distribution for the pile-up reweighting. Therefore a 5% systematic uncertainty for the default value of 69.2 mb [45] is added and propagated to the primary vertices distributions. The variation of the pile-up weight affects the signal and diboson background normalization in the signal region, resulting in an estimated uncertainty of 0.1%. For the pile-up no shape uncertainties are considered.

11.12 QCD scales

Weights are provided for each event for a variation of the QCD renormalization and factorization scales by a factor 2. The scales can be varied separately or together assuming a 100% correlation, taking the largest exclusion per event as the uncertainty.

The weight is propagated to the final distributions and the shape and normalization uncertainties are derived. The normalization uncertainties due to the QCD scales are shown in Fig. 42. The uncertainty on the signal normalization ranges between 3% and 15%. The QCD scales have a minimal effect ($< 0.1\%$) on the signal shape, therefore no shape uncertainties are considered.

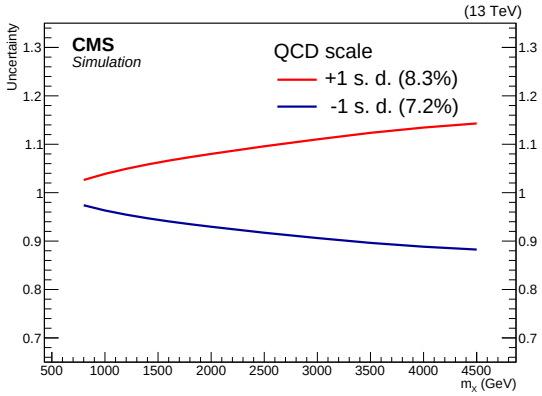

Figure 42: Normalization variations due to the QCD scales.

11.13 PDF scale

The systematic uncertainties for the PDF scale and acceptance are evaluated by varying the 100 weight distributions around their central value and propagating them as a normalization and shape uncertainty to the final distributions. The shape uncertainties due to the PDF scale and acceptance are shown in Figure 43. The effect on the signal acceptance is found to be around 0.5% and ranges between 8% and 30% for the scale.

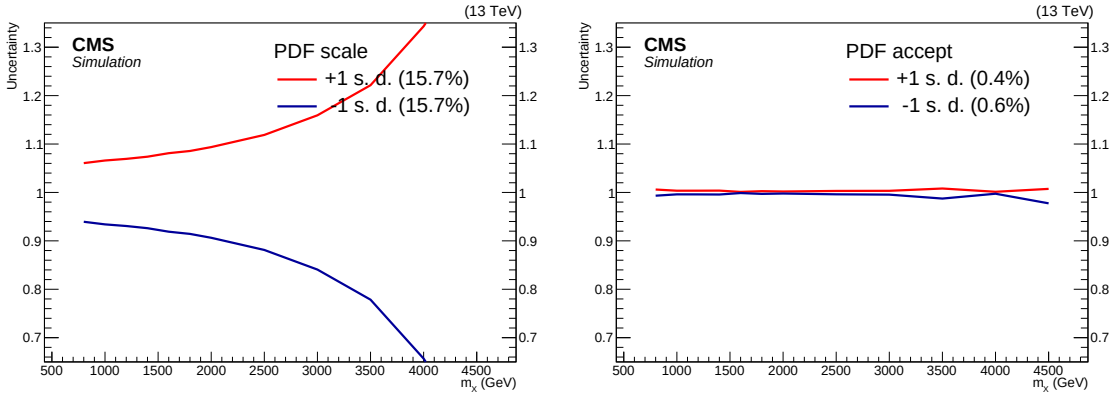

Figure 43: Shape variations due to PDF scale (left) and acceptance (right).

11.14 Uncertainties on the alpha

The background uncertainties, except the statistical uncertainty, are not propagated to the α-function, because the effect of most of them is correlated between sideband

and signal range and cancels out in the ratio. The remaining effects are smaller than the statistical uncertainty due to the limited simulation statistics. The statistical uncertainty is propagated to the uncertainties on the parameters of the V+jets functions. Figures 44-45 show the variation of the α-function due to the systematic uncertainties compared to the 1 and 2 sigma uncertainty bands originating from the statistical uncertainty, which are always larger than the effect of the systematic uncertainties.

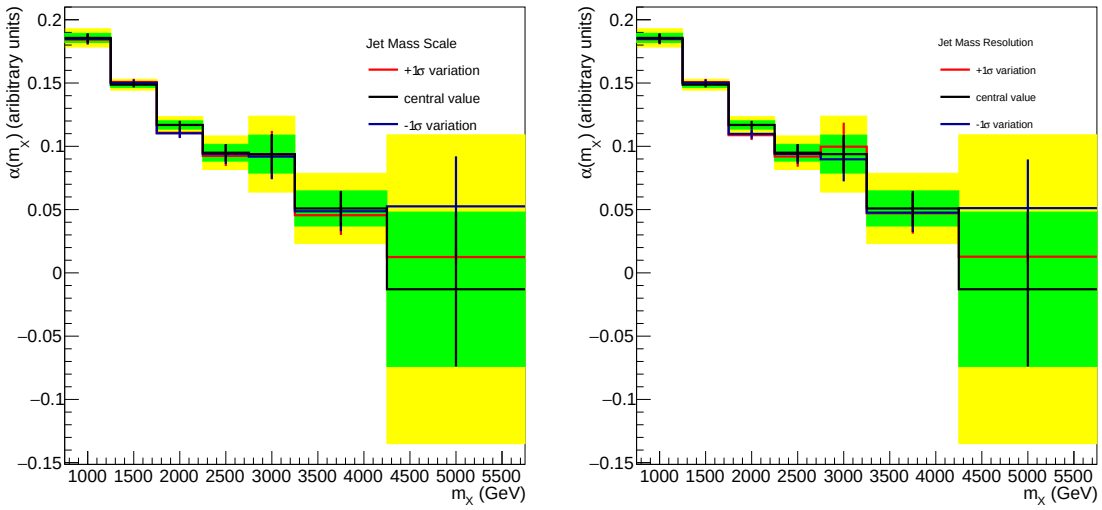

Figure 44: Variations of the (binned) α function after varying the jet mass scale (left) and resolution (right).

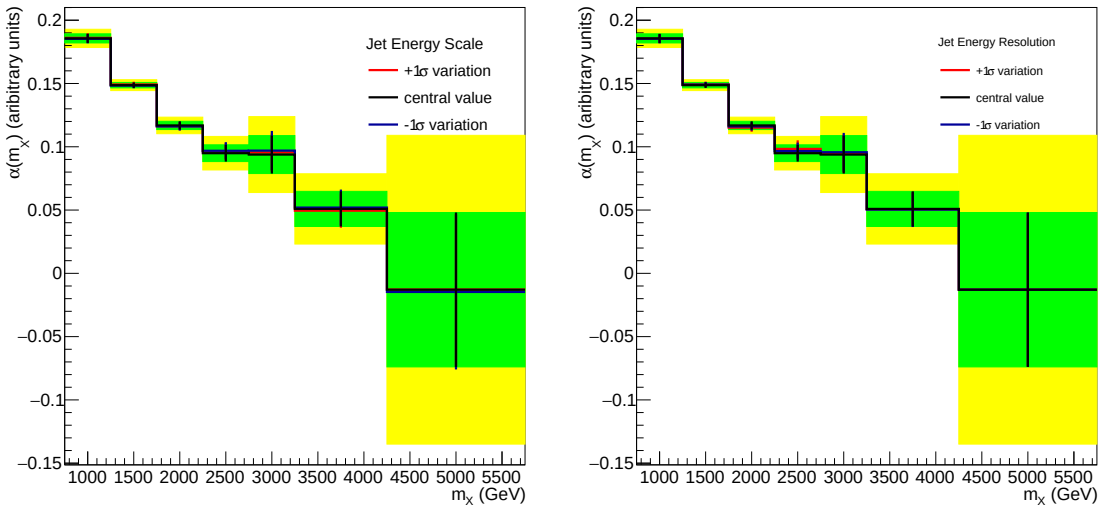

Figure 45: Variations of the (binned) α function after varying the jet energy scale (left) and resolution (right).

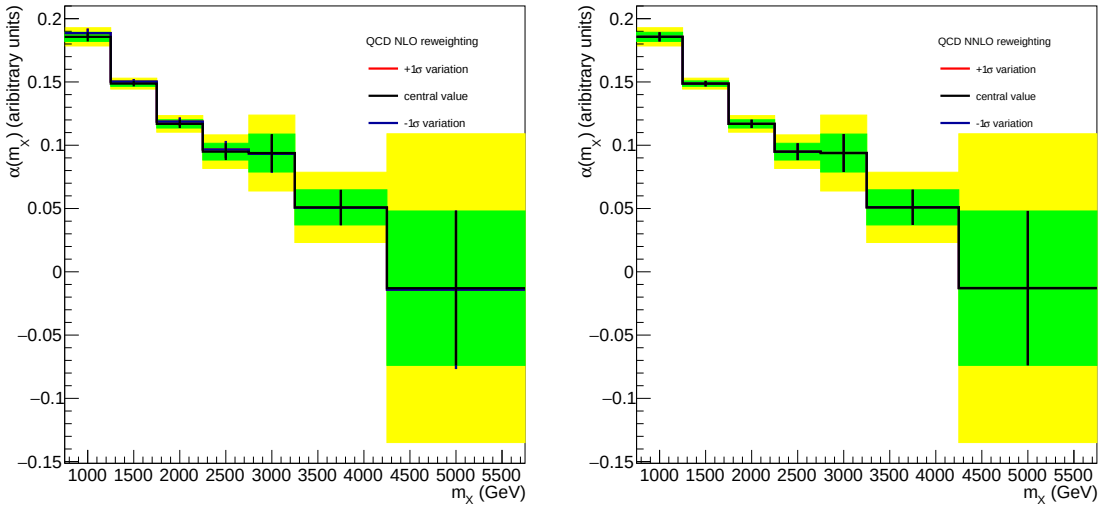

Figure 46: Variations of the (binned) α function after removing the QCD NLO (left) and QCD NNLO (right) corrections on the Z and W p_T spectra.

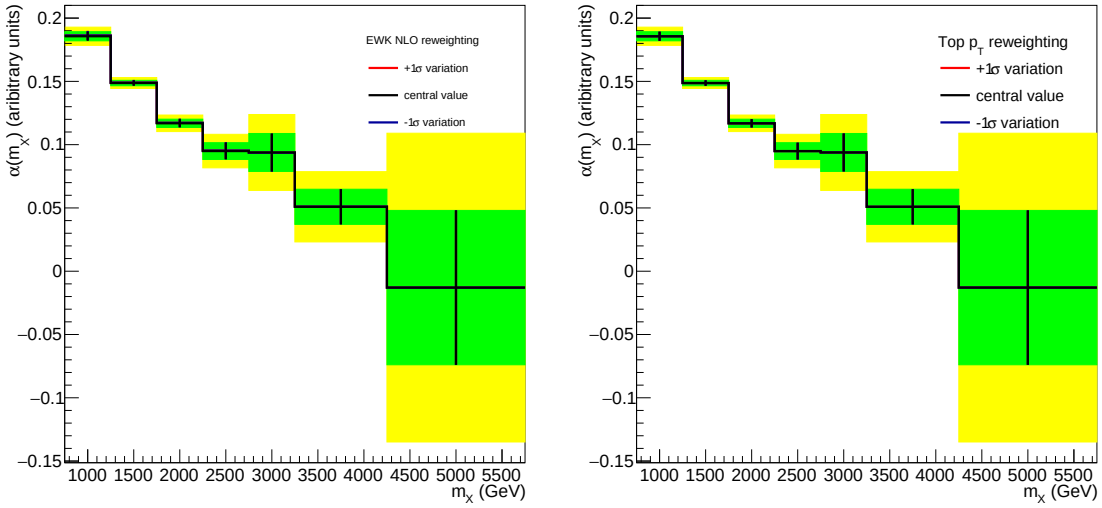

Figure 47: Variations of the (binned) α function after removing the EWK NLO correction on the Z and W p_T spectra (left) and the $t\bar{t}$ p_T reweighting (right).

11.15 Summary

The systematic uncertainties reported in this section are listed in Table 19. Additionally, a 2.5% uncertainty for luminosity is added [64][65][66].

	V+jets	$t\bar{t}$, t+X	VV	Signal
fit parameters†	✓	✓	✓	-
bkg. normalization	6–40%	-	-	-
top-quark scale factors	-	0.4–9.5%	-	-
jet energy scale †	-	-	3.0%	1.0%
jet energy resolution †	-	-	0.1%	0.1%
jet mass scale	-	-	0.6%	0.6%
jet mass resolution	-	-	9.0%	9.0%
electron Id, Iso	-	-	3.6%	
muon Id, Iso	-	-	4.9%	
lepton scale and res. †	-	-	-	1–3%
E_T^{miss} scale and res.	-	-	1%	1%
electron trigger	-	-	0.9%	
muon trigger	-	-	7%	
b-tagging	-	1.4% (0ℓ)	0.6% (0b), 6.5% (2b)	1-6% (0b), 4-15% (2b)
Higgs boson tagging	-	-	-	6%
pile-up	-	-	0.1%	0.1%
prefire	-	-	-	1%
QCD scale extrapolation	-	1.0%	-	-
QCD scales	-	-	18.9%	3–15% ‡
PDF scale	-	0.1%	4.7%	8–30% ‡
PDF acceptance	-	0.1%	0.2%	0.5%
luminosity	-	-	2.5%	2.5%

Table 19: Summary of systematic uncertainties for the background and signal samples. The entries labelled with † are also propagated to the shapes of the distributions. Uncertainties marked with ‡ impact to the signal cross section. Uncertainties in the same line are treated as correlated. The uncertainties except luminosity are correlated between years.

12 Results

The search for a signal is conducted by testing the signal plus background hypothesis against the background-only hypothesis. In order to quantify the agreement between the observed data and a given hypothesis a function called a test statistic is constructed. The test statistic chosen is a profile likelihood ratio $\tilde{q}$ and is derived from a combined signal and background fit to the unbinned m_X distribution. The systematic uncertainties are treated as nuisance parameters and profiled in the fit. The profile likelihood can be calculated with the formula:

$$\mathcal{L}(\text{data}|\mu,\theta) = \prod_i \frac{\gamma_i^{n_i} \cdot e^{-\gamma_i}}{n_i!} \qquad \text{with} \qquad \gamma_i = \mu S_i(\theta) + B_i(\theta),$$

where $S_i(\theta)$ and $B_i(\theta)$ are the signal and background events in the i-th bin, μ is the signal strength and θ the nuisance parameters. The profile likelihood ratio used as the test statistics is defined as:

$$\tilde{q}(\mu) = -2\text{log}\frac{\mathcal{L}(\text{data}|\mu,\hat{\theta}_\mu)}{\mathcal{L}(\text{data}|\hat{\mu},\hat{\theta}_{\hat{\mu}})},$$

where the values $\hat{\mu}, \hat{\theta}_\mu$ and $\hat{\theta}_{\hat{\mu}}$ are fixed to their best-fit value. In order to decide if the observed data agrees with the signal plus background or the background-only hypothesis, the p value can be used. The p value represents the probability to have a value of $\tilde{q}$ with equal or lesser compatibility with the corresponding hypothesis than the observed $\tilde{q}$, and is derived from analytical functions using the asymptotic approximation [67]. A discovery is claimed if the background-only p-value is less than 5 sigma, which corresponds to a value of $p_b = 0.0000003$. If no significant deviation from the background-only hypothesis is found, the upper limit on the signal strength is derived with the 95% CL_s criterion, defined as

$$CL_s = \frac{CL_{s+b}}{CL_b} = \frac{p_{s+b}}{1-p_b},$$

such that $CL_s(\mu) = 0.05$.

The observed upper limit on the resonance cross section times $\mathcal{B}(Z' \to ZH)$, as well as the expected limit and its relative 68% and 95% uncertainty bands, are reported as a function of the resonance mass in Figures 48-53 for all categories. The Figures are showing the best sensitivity for the 0ℓ, 2 b-tagging categories. The VBF categories do not have enough statistics by themselves to exclude any range of mass. The Figures 54,55 and 56 show the exclusion limits with categories combined. In Figure 56 the results from the $Z' \to ZH$ search using 2016 data are added as a comparison [1]. The exclusion limits show no significant excess. The mass range below 3.4 and 3.7 TeV can be excluded at a 95% confidence level if the resonance couples predominantly to fermions and bosons, respectively. The upper limit of the excluded mass range is increased by 1.3-1.4 TeV depending on the model as compared to the 2016 search. If the heavy resonances couple only to the SM bosons, a Z' cross section smaller than 0.4-24 fb is excluded, depending on the Z' mass.

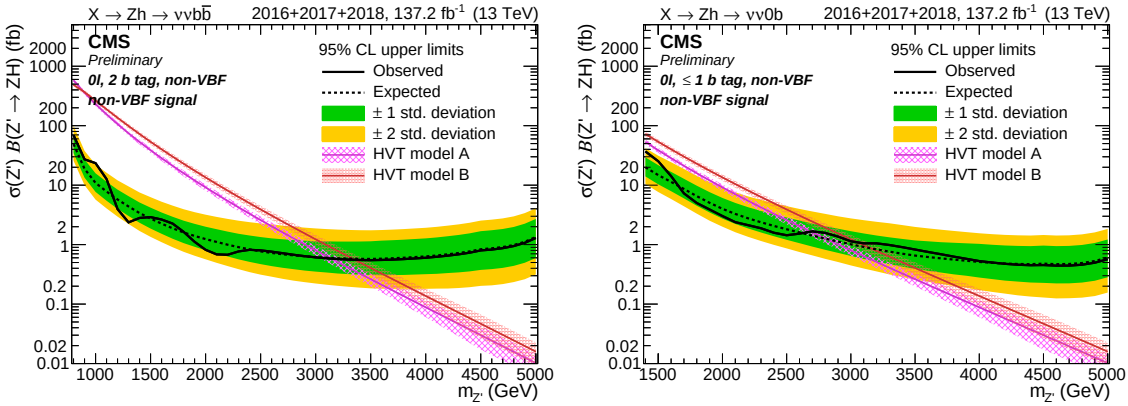

Figure 48: Observed and expected (with $\pm 1(2)\sigma$ band) 95%C.L. upper limit on $\sigma \times \mathcal{B}(Z' \to ZH)$ in the 0ℓ, 2 b-tagging (left) and $\leq$1 b-tagging (right) category for the non-VBF signal, including all statistical and systematics uncertainties.

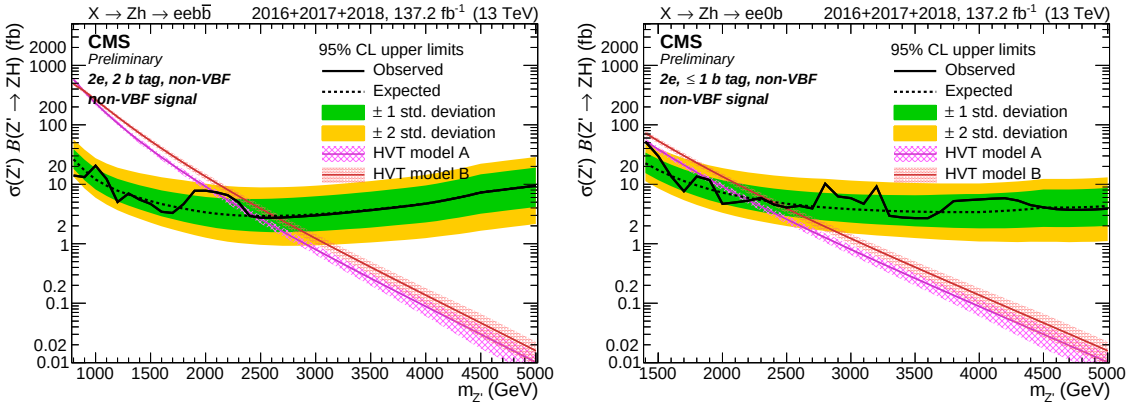

Figure 49: Observed and expected (with $\pm 1(2)\sigma$ band) 95%C.L. upper limit on $\sigma \times \mathcal{B}(Z' \to ZH)$ in the $2e$, 2 b-tagging (left) and $\leq$1 b-tagging (right) category for the non-VBF signal, including all statistical and systematics uncertainties.

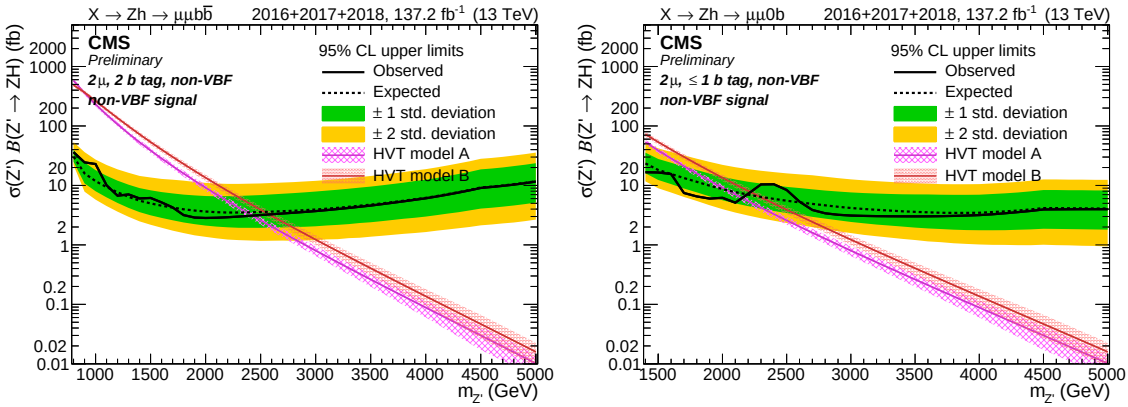

Figure 50: Observed and expected (with $\pm 1(2)\sigma$ band) 95%C.L. upper limit on $\sigma \times \mathcal{B}(Z' \to ZH)$ in the 2μ, 2 b-tagging (left) and $\leq$1 b-tagging (right) category for the non-VBF signal, including all statistical and systematics uncertainties.

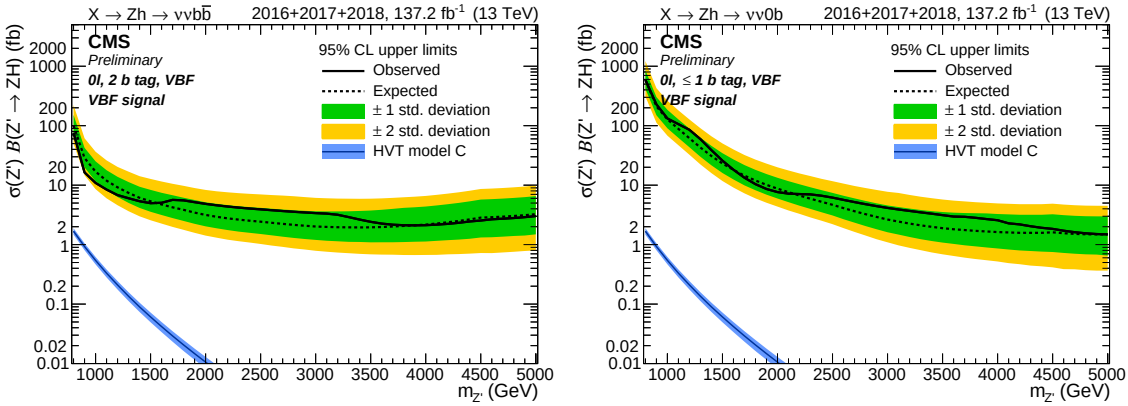

Figure 51: Observed and expected (with $\pm 1(2)\sigma$ band) 95%C.L. upper limit on $\sigma \times \mathcal{B}(Z' \to ZH)$ in the 0ℓ, VBF 2 b-tagging (left) and $\leq$1 b-tagging (right) category for the VBF signal, including all statistical and systematics uncertainties.

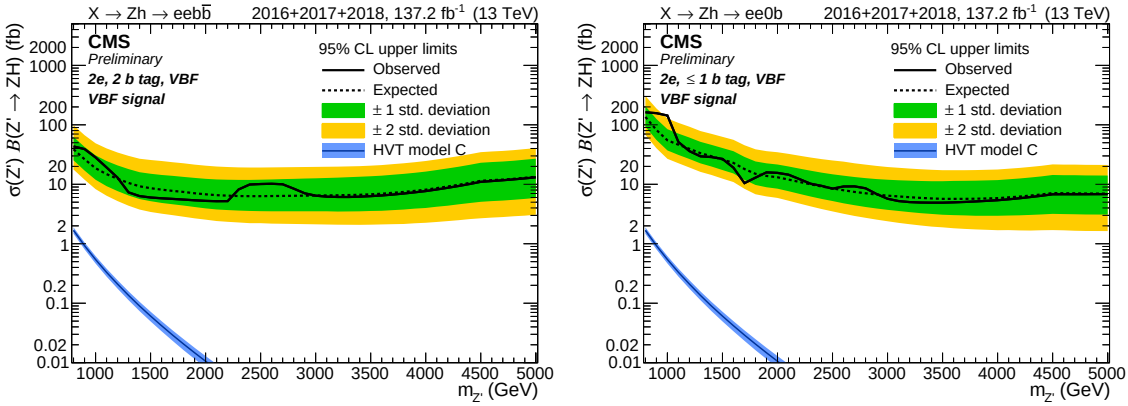

Figure 52: Observed and expected (with $\pm 1(2)\sigma$ band) 95%C.L. upper limit on $\sigma \times \mathcal{B}(Z' \to ZH)$ in the $2e$, VBF 2 b-tagging (left) and $\leq$1 b-tagging (right) category for the VBF signal, including all statistical and systematics uncertainties.

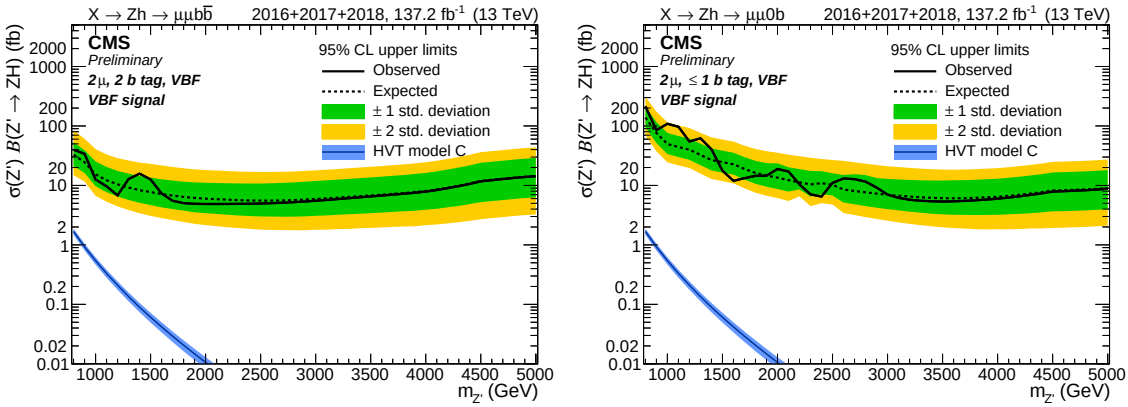

Figure 53: Observed and expected (with $\pm 1(2)\sigma$ band) 95%C.L. upper limit on $\sigma \times \mathcal{B}(Z' \to ZH)$ in the 2μ, VBF 2 b-tagging (left) and $\leq$1 b-tagging (right) category for the VBF signal, including all statistical and systematics uncertainties.

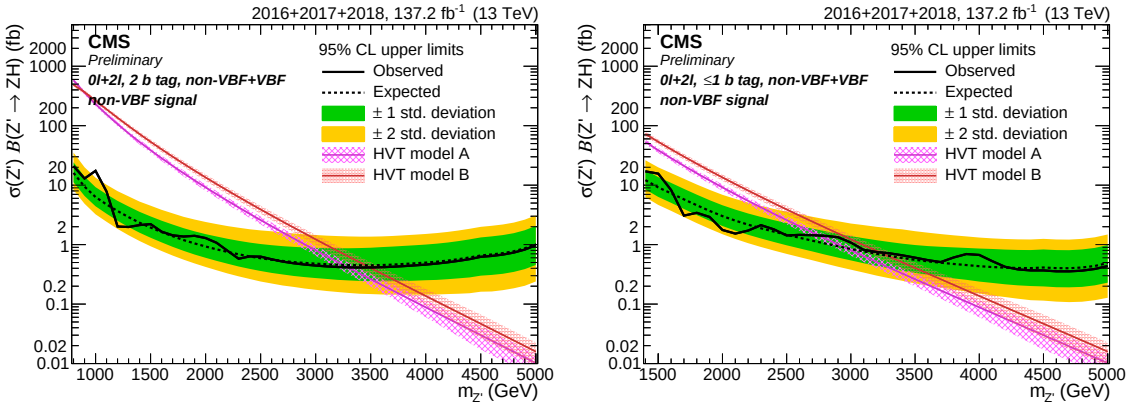

Figure 54: Observed and expected (with $\pm 1(2)\sigma$ band) 95%C.L. upper limit on $\sigma \times \mathcal{B}(Z' \to ZH)$ in the 2 b-tagging combined (left) and $\leq$1 b-tagging combined (right) category for the non-VBF signal, including all statistical and systematics uncertainties.

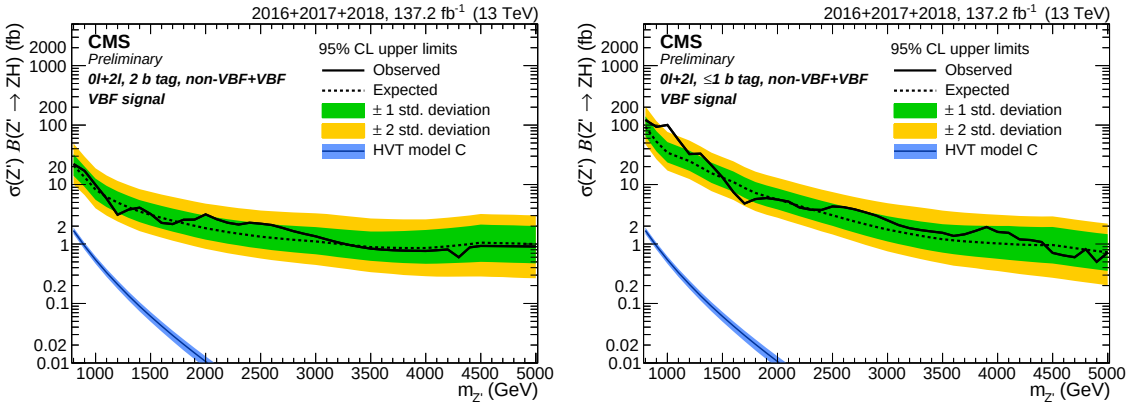

Figure 55: Observed and expected (with $\pm 1(2)\sigma$ band) 95%C.L. upper limit on $\sigma \times \mathcal{B}(Z' \to ZH)$ in the 2 b-tagging combined (left) and $\leq$1 b-tagging combined (right) category for the VBF signal, including all statistical and systematics uncertainties.

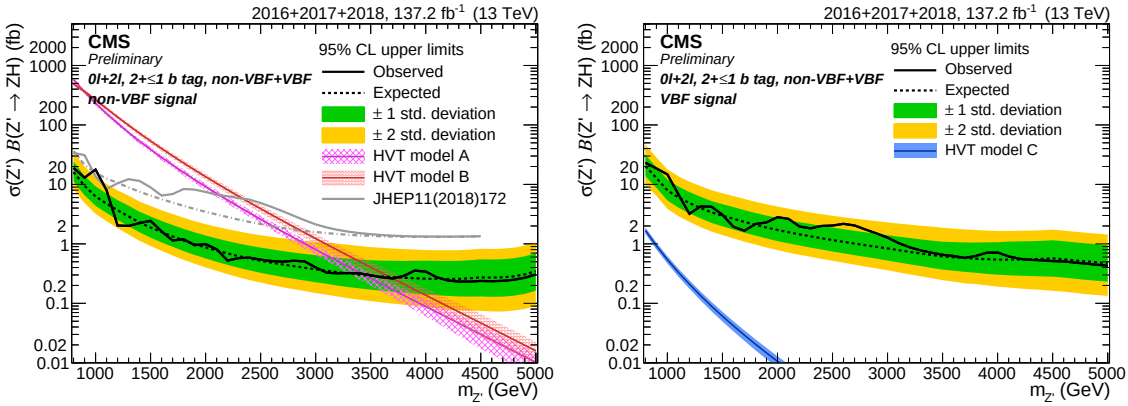

Figure 56: Observed and expected (with $\pm 1(2)\sigma$ band) 95%C.L. upper limit on $\sigma \times \mathcal{B}(Z' \to ZH)$ in the categories combined for the non-VBF signal (left) and the VBF signal (right), including all statistical and systematics uncertainties.

13 Summary

This thesis describes the search for a heavy resonance with a mass between 800 and 5000 GeV and decaying into a Higgs and a Z boson as predicted by the heavy-vector-triplet model, which provides a solution to the hierarchy problem. The signal is either produced through $q\bar{q}$ annihilation or through vector boson fusion. The investigated decay modes include the leptonic decays of the Z boson to a pair of neutrinos, electrons or muons and the Higgs boson decaying into $b\bar{b}$ or the inclusive decay channel. The data used for this search was recorded at a center of mass energy of $\sqrt{s} = 13$ TeV by the CMS detector from 2016 to 2018 and amounts to an integrated luminosity of 137.2 fb^{-1}. The main source of background originates from vector bosons in association with jets, while minor contributions arise from top quark pairs, single top quarks and pairs of vector bosons. The background estimation of the mass distribution used to search for the heavy resonance is estimated with a transfer function, which is derived from simulated events from signal-enriched and signal-depleted regions in the jet-mass distribution. The V+jets background normalization is extracted from data in the signal-depleted region and the shape is determined from data in the signal-depleted region and extrapolated to the signal-enriched region with the transfer function. The top-quark contribution is normalized with data using top-quark scale factors, derived with top-quark control regions selecting an almost pure $t\bar{t}$ sample. The shape of the top-quark contribution and normalization and shape of the diboson background are taken from simulation. Systematic uncertainties with impacts on the normalization and shape of the signal and background models are considered. The signal plus background hypothesis is tested against the background-only hypothesis using a profile likelihood ratio and deriving 95% confidence level upper limits on the signal strength. No evidence of significant deviations from the background-only hypothesis were found. The mass range below 3.4 and 3.7 TeV can be excluded at a 95% confidence level if the resonance couples predominantly to fermions and bosons, respectively. If the heavy resonances couple only to the SM bosons, a Z' cross section smaller than 0.4-24 fb is excluded, depending on the Z' mass.

References

[1] CMS Collaboration. Search for heavy resonances decaying into a vector boson and a Higgs boson in final states with charged leptons, neutrinos, and b quarks at $\sqrt{s} = 13$ TeV. *JHEP*, 11:172, 2018.

[2] ATLAS Collaboration. Search for new resonances decaying to a w or z boson and a higgs boson in the $\ell^+\ell^- b\bar{b}$, $\ell\nu b\bar{b}$, and $\nu\bar{\nu}b\bar{b}$ channels with pp collisions at $\sqrt{s} = 13$ tev with the atlas detector. *Physics Letters B*, 765:32, 2017.

[3] P. W. Higgs. Broken symmetries and the masses of gauge bosons. *Phys. Rev. Lett.*, 13:508–509, 1964.

[4] F. Englert and R. Brout. Broken symmetry and the mass of gauge vector mesons. *Phys. Rev. Lett.*, 13:321–323, 1964.

[5] G. S. Guralnik, C. R. Hagen, and T. W. B. Kibble. Global conservation laws and massless particles. *Phys. Rev. Lett.*, 13:585–587, 1964.

[6] CMS Collaboration. Observation of a new boson at a mass of 125 GeV with the CMS experiment at the LHC. *Phys. Lett. B*, 716:30, 2012.

[7] ATLAS Collaboration. Observation of a new particle in the search for the standard model higgs boson with the ATLAS detector at the LHC. *Phys. Lett. B.*, 716:1–29, 2012.

[8] Wikimedia Commons. File: Standard model of elementary particles.svg, 2020.

[9] LHC Higgs Cross Section Working Group. File: Higgs BR LM, 2020.

[10] CMS Collaboration. Inclusive search for a highly boosted higgs boson decaying to a bottom quark-antiquark pair. *Phys. Rev. Lett.*, 120:071802, 2018.

[11] CMS Collaboration. Search for the associated production of the higgs boson with a top-quark pair. *JHEP*, 9, 2014.

[12] CMS Collaboration. Search for the standard model higgs boson produced through vector boson fusion and decaying to bb. *Phys. Rev. D*, 92:032008, 2015.

[13] CMS Collaboration. Observation of higgs boson decay to bottom quarks. *Phys. Rev. Lett.*, 121, 2018.

[14] ATLAS Collaboration. Observation of htobb decays and vh production with the atlas detector. *Phys. Lett. B*, 786:59, 2018.

[15] Roberto Contino, Duccio Pappadopulo, David Marzocca, and Riccardo Rattazzi. On the effect of resonances in composite higgs phenomenology. *Journal of High Energy Physics*, 2011(10):1–50, 2011.

[16] David Marzocca, Marco Serone, and Jing Shu. General composite higgs models. *Journal of High Energy Physics*, 2012(8):1–52, 2012.

[17] Brando Bellazzini, Csaba Csaki, and Javi Serra. Composite Higgses. *Eur. Phys. J.*, C74(5):2766, 2014.

[18] Tao Han, Heather E. Logan, Bob McElrath, and Lian-Tao Wang. Phenomenology of the little Higgs model. *Phys. Rev.*, D67:095004, 2003.

[19] Martin Schmaltz and David Tucker-Smith. Little higgs theories. *Annual Review of Nuclear and Particle Science*, 55(1):229–270, 2005.

[20] Maxim Perelstein. Little higgs models and their phenomenology. *Progress in Particle and Nuclear Physics*, 58(1):247 – 291, 2007.

[21] Y. Nambu. Quasi-particles and gauge invariance in the theory of superconductivity. *Phys. Rev.*, 117:648, 1960.

[22] J. Goldstone. Field theories with superconductor solutions. *Nuovo Cim*, 19:154, 1961.

[23] J. Goldstone, A. Salam, and S. Weinberg. Broken symmetries. *Phys. Rev.*, 127:965, 1962.

[24] S. Weinberg. *The Quantum Theory of Fields*, volume 2. Cambridge University Press, 1996.

[25] D. Pappadopulo, A. Thamm, R. Torre, and A. Wulzer. Heavy vector triplets: bridging theory and data. *JHEP*, 09:60, 2014.

[26] CMS Collaboration. The CMS experiment at the CERN LHC. *JINST*, 03:S08004, 2008.

[27] ATLAS Collaboration. The ATLAS collaboration at the CERN Large Hadron Collider. *JINST*, 3:S08003, 2008.

[28] LCHb Collaboration. The LHCb detector at the LHC. *JINST*, 3:S08005, 2008.

[29] ALICE Collaboration. The ALICE experiment at the CERN LHC. *JINST*, 3:S08002, 2008.

[30] Wikimedia Commons. File: LHC.svg, 2020.

[31] M. Lipinski. The phase-1 upgrade of the CMS pixel detector. *JINST*, 12:C07009, 2017.

[32] CMS Collaboration. Description and performance of track and primary-vertex reconstruction with the cms tracker. *JINST*, 9:P10009, 2014.

[33] A Dominguez, D Abbaneo, K Arndt, N Bacchetta, A Ball, E Bartz, W Bertl, G M Bilei, G Bolla, H W K Cheung, M Chertok, S Costa, N Demaria, Daniel Dominguez Vazquez, K Ecklund, W Erdmann, K Gill, G Hall, K Harder, F Hartmann, R Horisberger, W Johns, H C Kaestli, K Klein, D Kotlinski, S Kwan, M Pesaresi, H Postema, T Rohe, C Schäfer, A Starodumov, S Streuli, A Tricomi, P Tropea, J Troska, F Vasey, and W Zeuner. CMS Technical Design Report for the Pixel Detector Upgrade. Technical Report CERN-LHCC-2012-016, CMS-TDR-11, CERN, Sep 2012.

[34] CMS Collaboration. Jet energy scale and resolution in the cms experiment in pp collisions at 8 tev. *JINST*, 12:P02014, 2017.

[35] CMS Collaboration. The performance of the CMS muon detector in proton-proton collisions at $\sqrt{s} = 7$ tev at the lhc. *JINST*, 8:P11002, 2013.

[36] CMS Collaboration. Performance of CMS Muon Reconstruction in *pp* Collision Events at $\sqrt{s} = 7$ TeV. *JINST*, 7:P10002, 2012.

[37] Darin Acosta for the CMS Collaboration. CMS Trigger Improvements Towards Run II. *Nuclear and Particle Physics Proceedings*, 273-275:1008–1013, 2016.

[38] CMS Collaboration. Public cms luminosity information, 2019.

[39] Particle Data Group, J. Beringer, et al. Review of Particle Physics. *Phys. Rev. D*, 86:010001, 2012.

[40] J. M. Lindert, S. Pozzorini, R. Boughezal, J. M. Campbell, A. Denner, S. Dittmaier, A. Gehrmann-De Ridder, T. Gehrmann, N. Glover, A. Huss, S. Kallweit, P. Maierhöfer, M. L. Mangano, T. A. Morgan, A. Mück, F. Petriello, G. P. Salam, M. Schönherr, and C. Williams. Precise predictions for v+jets dark matter backgrounds. *Eur. Phys. J. C*, 77:829, 2017.

[41] CMS Collaboration. Particle-flow reconstruction and global event description with the CMS detector. *JINST*, 12:P10003, 2017.

[42] CMS Collaboration. Performances of E_T^{miss} trigger for heavy diboson searches in 2017 data. CMS Note 2017/045, CERN, 2017.

[43] CMS Collaboration. Performances of E_T^{miss} trigger for heavy diboson searches in 2018 data. CMS Note 2018/048, CERN, 2018.

[44] A. Rizzi, S. Donato, P. Azzurri. Primary vertex sorting. Technical report, CERN, 2015.

[45] CMS Collaboration. Pileup reweighting procedure - https://twiki.cern.ch/twiki/bin/viewauth/cms/pileupreweighting.

[46] CMS Collaboration. Utilities for accessing pileup information for data - https://twiki.cern.ch/twiki/bin/view/cms/pileupjsonfilefordata.

[47] CMS Collaboration. EGamma POG - Cut based electron ID for Run2 - https://twiki.cern.ch/twiki/bin/view/CMS/CutBasedElectronIdentificationRun2.

[48] Vardan Khachatryan et al. Performance of electron reconstruction and selection with the CMS detector in proton-proton collisions at $\sqrt{s} = 8TeV$. *JINST*, 10:P06005, 2015.

[49] Serguei Chatrchyan et al. Performance of CMS muon reconstruction in *pp* collision events at $\sqrt{s} = 7$ TeV. *JINST*, 7:P10002, 2012.

[50] CMS Collaboration. Reference muon id, isolation and trigger efficiencies for Run-II - https://twiki.cern.ch/twiki/bin/view/CMS/MuonReferenceEffsRun2.

[51] CMS Collaboration. Performance of reconstruction and identification of τ leptons decaying to hadrons and ν_τ in pp collisions at $\sqrt{s} = 13$ tev. *JINST*, 13(10):P10005, 2018.

[52] CMS Collaboration. Pileup Removal Algorithms. Technical Report CMS-PAS-JME-14-001, CERN, Geneva, 2014.

[53] Daniele Bertolini, Philip Harris, Matthew Low, and Nhan Tran. Pileup per particle identification. *Journal of High Energy Physics*, 2014(10):59, 2014.

[54] R. Salam. Fastjet package. Technical report, CNRS, 2011.

[55] Matteo Cacciari, Gavin P. Salam, and Gregory Soyez. The anti-k_t jet clustering algorithm. *JHEP*, 04:063, 2008.

[56] Andrew J. Larkoski, Simone Marzani, Gregory Soyez, and Jesse Thaler. Soft Drop. *JHEP*, 05:146, 2014.

[57] CMS Collaboration. Measurement of $\mathrm{B\overline{B}}$ angular correlations based on secondary vertex reconstruction at $\sqrt{s} = 7\,\mathrm{TeV}$. *JHEP*, 03:136, 2011.

[58] Nazar Bartosik. File: B-tagging diagram.png, 2020.

[59] Serguei Chatrchyan et al. Identification of b-quark jets with the CMS experiment. *JINST*, 8:P04013, 2013.

[60] CMS Collaboration. Identification of b quark jets at the CMS Experiment in the LHC Run 2. Technical Report CMS-PAS-BTV-15-001, CERN, Geneva, 2016.

[61] CMS Collaboration. Particle-flow event reconstruction in CMS and performance for jets, taus, and E_T^{miss}. CMS Physics Analysis Summary CMS-PAS-PFT-09-001, CERN, 2009.

[62] CMS Collaboration. Reference measurements and calibrations for Run-II - https://twiki.cern.ch/twiki/bin/view/CMS/MuonReferenceSelectionAndCalibrationsRun2.

[63] CMS Collaboration. Recommendation for using b-tag objects in physics analyses, 2019.

[64] CMS Collaboration. CMS Luminosity Measurement for the 2016 Data Taking Period. Technical Report CMS-PAS-LUM-17-001, CERN, Geneva, 2016.

[65] CMS Collaboration. CMS luminosity measurement for the 2017 data-taking period at $\sqrt{s} = 13$ TeV. Technical Report CMS-PAS-LUM-17-004, CERN, Geneva, 2017.

[66] CMS Collaboration. CMS luminosity measurement for the 2018 data-taking period at $\sqrt{s} = 13$ TeV. Technical Report CMS-PAS-LUM-18-002, CERN, Geneva, 2018.

[67] Glen Cowan, Kyle Cranmer, Eilam Gross, and Ofer Vitells. Asymptotic formulae for likelihood-based tests of new physics. *The European Physical Journal C*, 71(2), 2011.